



# Facile synthesis and application of CdS/Bi<sub>20</sub>TiO<sub>32</sub>/Bi<sub>4</sub>Ti<sub>3</sub>O<sub>12</sub> ternary heterostructure: A synergistic multi-heterojunction photocatalyst for enhanced endosulfan degradation and hydrogen evolution reaction

Krishnendu Das <sup>a</sup>, Ranjit Bariki <sup>a</sup>, Dibyananda Majhi <sup>a</sup>, Abtar Mishra <sup>b</sup>, Kundan K. Das <sup>c</sup>, Rohan Dhiman <sup>b</sup>, B.G. Mishra <sup>a,\*</sup>

<sup>a</sup> Department of Chemistry, National Institute of Technology, Rourkela 769008, Odisha, India

<sup>b</sup> Department of Life Science, National Institute of Technology, Rourkela 769008, Odisha, India

<sup>c</sup> Centre for Nano Science and Nano Technology, Siksha 'O' Anusandhan (Deemed to be University), Bhubaneswar 751030, India



## ARTICLE INFO

### Keywords:

Multi-heterojunctions  
Bismuth titanate  
CdS  
Endosulfan  
MTT assay  
Hydrogen evolution

## ABSTRACT

Facile fabrication of visible light responsive multicomponent heterostructure photocatalysts with synergistic photoelectron migration is an effective approach with potential application in water remediation and renewable energy generation. In this study, a series of ternary multi-heterojunction CdS/Bi<sub>20</sub>TiO<sub>32</sub>/Bi<sub>4</sub>Ti<sub>3</sub>O<sub>12</sub> (CdSxBTC) photocatalysts were prepared by hydrothermal deposition of CdS nanoparticles (15–25 nm) over one pot combustion synthesized Bi<sub>20</sub>TiO<sub>32</sub>/Bi<sub>4</sub>Ti<sub>3</sub>O<sub>12</sub> (BTC) nanostructures. Comprehensive characterization of the ternary composites revealed enhanced optical absorption, high interfacial contact, fast electron channelization and a prolonged excited state life time. The CdSxBTC composite materials displayed enhanced photocatalytic activity for endosulfan degradation ( $k_{app}$  value 6–12 times greater than pure semiconductors) and water splitting reaction (H<sub>2</sub> production rate 1890  $\mu\text{mol g}^{-1}\text{h}^{-1}$  and apparent conversion efficiency 19%). The cell viability -study disclosed non-cytotoxic nature of the treated endosulfan solution. A synergistic Type-I bridged coupled Z-scheme electron migration process accounted for robust radical generation ability ( $\bullet\text{O}_2^-$  and  $\bullet\text{OH}$ ) and photocatalytic activity of the ternary composites.

## 1. Introduction

Rational design of semiconductor heterostructure photocatalysts with broad spectrum response in visible region is a promising field of research with potential application prospects in renewable energy production and environmental remediation [1–6]. The heterostructure materials display improved optical absorption, facile charge transport properties and resistance to charge recombination in comparison to a pristine semiconductor. By adopting suitable preparative strategy many novel heterostructure photocatalysts have been designed in recent past which show excellent activity towards aqueous as well as vapor phase photodegradation of micropollutants [7–10]. For instance, the H-Zr<sub>0.1</sub>Tl<sub>0.9</sub>O<sub>2</sub>@UiO-66-NH<sub>2</sub> heterostructure prepared by an “Interfacial metal interpenetration” strategy exhibits excellent interface compatibility for charge carrier migration which plays a vital role in vapor phase photodegradation of acetaldehyde [8]. In the quest for preparation of novel photocatalyst with enhanced optoelectronic

features, several binary heterostructure materials with different electron migration schemes including Type-I, Type-II, Z-scheme and S-scheme heterostructure have been reported in literature [1–4,6,11–13]. Among them, the biomimetic Z-scheme heterostructure materials are characterized by their optimal redox ability and higher charge carrier separation property [4,11,14–16]. In a Z-scheme heterostructure, the less reducing CB photoelectrons of one semiconductor component recombine with the less oxidizing VB holes of another semiconductor leaving aside the more reactive electrons and holes for utilization in photocatalytic processes [4,16]. In recent years, there is significant research effort to prepare novel Z-scheme ternary heterostructure materials with prolonged excited state lifetime, improved photoelectrochemical properties and higher number of active redox sites for photocatalytic application. Some of the recently studied ternary Z-scheme heterostructures include Ag/Ag<sub>3</sub>VO<sub>4</sub>/g-C<sub>3</sub>N<sub>4</sub>, Bi<sub>2</sub>S<sub>3</sub>/BiVO<sub>4</sub>/MgIn<sub>2</sub>S<sub>4</sub>, Bi<sub>2</sub>S<sub>3</sub>/MoS<sub>2</sub>/TiO<sub>2</sub>, CdS/g-C<sub>3</sub>N<sub>4</sub>/RGO, g-C<sub>3</sub>N<sub>4</sub>/Ag<sub>3</sub>VO<sub>4</sub>/rGO, Mo<sub>2</sub>C/MoS<sub>2</sub>/In<sub>2</sub>S<sub>3</sub>, WO<sub>3</sub>/g-C<sub>3</sub>N<sub>4</sub>/Bi<sub>2</sub>O<sub>3</sub> and ZnMoO<sub>4</sub>/BiFeWO<sub>6</sub>/rGO which show promising

\* Corresponding Author.

E-mail address: [brajam@nitrkl.ac.in](mailto:brajam@nitrkl.ac.in) (B.G. Mishra).

application potential for degradation of pharmaceutical contaminants, pesticides, reduction of heavy metals,  $\text{CO}_2$  reduction and  $\text{H}_2$  evolution reactions [17–24]. In a multicomponent heterostructure system, the synergistic channelization of photoelectrons is an important parameter which can ensure efficient space separation of electron-hole pairs. Such heterostructures can contain assorted microscopic heterojunctions between the photoactive components which can function through multi-interfacial electron transfer paths leading to efficient charge channelization. In recent past, we have reported the one step synthesis and visible light assisted photocatalytic application of  $\text{CdS}/\text{BiOBr}/\text{Bi}_2\text{O}_2\text{CO}_3$  and  $\text{Bi}_2\text{S}_3/\beta\text{-Bi}_2\text{O}_3/\text{ZnIn}_2\text{S}_4$  dual Z-scheme ternary composite towards degradation of agrochemical and pharmaceutical contaminants,  $\text{Cr(VI)}$  reduction and bacterial inactivation [25,26]. In continuation of our interest to develop Bi-based novel ternary heterostructure materials with improved optoelectronic features, in this work we have reported the facile synthesis and photocatalytic application of a coupled Z-scheme  $\text{CdS}/\text{Bi}_{20}\text{TiO}_{32}/\text{Bi}_4\text{Ti}_3\text{O}_{12}$  ternary composite.

Bismuth titanates (Bi-Ti-O) are a class of fascinating semiconductor oxides which show unique photophysical behavior and exist in a variety of crystallographic forms with different photonic excitation energy [27–31]. From the point of view of photocatalytic applications,  $\text{Bi}_4\text{Ti}_3\text{O}_{12}$  (layered perovskite),  $\text{Bi}_2\text{Ti}_2\text{O}_7$  (pyrochlore),  $\text{Bi}_{12}\text{TiO}_{20}$  (Sillenite) and  $\text{Bi}_{20}\text{TiO}_{32}$  (isostructural to  $\beta\text{-Bi}_2\text{O}_3$ ) have been explored as promising candidates for  $\text{H}_2$  and  $\text{O}_2$  evolution reactions, selective reduction of  $\text{CO}_2$  and degradation of refractory organic contaminants from aqueous sources [28–32].  $\text{Bi}_4\text{Ti}_3\text{O}_{12}$  (BT) is an Aurivillius phase n-type semiconducting oxide which possess important physicochemical attributes including a layer structure, strong intra-electric field and a highly dispersed valance band for easy migration of holes [14,29,31].  $\text{Bi}_4\text{Ti}_3\text{O}_{12}$  displays limited absorption in visible region and a higher charge recombination rate which limits its application in photocatalytic reactions. On the other hand,  $\text{Bi}_{20}\text{TiO}_{32}$  (BTO) is a visible light active semiconductor (band gap: 2.3–2.4 eV) which is a metastable phase and poses many challenges during its synthesis [32]. The conventional synthesis methods including high temperature solid state synthesis invariably lead to the formation Sillenite  $\text{Bi}_{12}\text{TiO}_{20}$  phase [33]. The BTO is usually observed as an impurity phase during the synthesis of  $\text{Bi}_2\text{Ti}_2\text{O}_7$  pyrochlore and rapidly transforms to  $\text{Bi}_2\text{Ti}_2\text{O}_7$  at temperature beyond 500 °C. The selective synthesis of BTO has been accomplished under specific conditions such as high temperature rapid quenching, solvothermal synthesis using benzyl alcohol and wet chemical route at 1MPa  $\text{N}_2$  pressure [33–35]. Both BT and BTO possess highly '+ ve' valance band maximum (VBM) (> 2.5 eV) which can generate strongly oxidizing  $\bullet\text{OH}$  radicals in aqueous suspension. Thus a multicomponent photosystem containing both BT and BTO is expected to generate more number of redox sites for photocatalytic oxidation reaction [14,29,32]. Although, bismuth titanates based heterostructures involving different phases of Bi-Ti-O system such as  $\text{Bi}_{12}\text{TiO}_{20}/\text{Bi}_4\text{Ti}_3\text{O}_{12}$ ,  $\text{Bi}_2\text{Ti}_2\text{O}_7/\text{Bi}_4\text{Ti}_3\text{O}_{12}$  and  $\text{Bi}_4\text{Ti}_3\text{O}_{12}/\text{Bi}_2\text{O}_3/\text{Bi}_{12}\text{TiO}_{20}$  have been studied [30,36,37], there is no report on preparation and photocatalytic application of  $\text{Bi}_{20}\text{TiO}_{32}/\text{Bi}_4\text{Ti}_3\text{O}_{12}$  heterostructure material. Moreover, rapid one pot synthesis of the composite by using a simple and less time consuming preparation method is yet to be explored. Judiciously combining these semiconductors with metal sulfide nanoparticles can lead to formation of Z-scheme heterojunctions with high charge separation potency. Metal sulfides due to their low band gap, substantial visible light absorption and highly '-ve' conduction band minimum (CBM) are ideal choice for construction of Z-scheme heterojunction with bismuth titanate based semiconductors [25,26,38]. Cadmium sulfide ( $\text{CdS}$ ) is a promising n-type low band gap semiconductor which has been extensively studied for many important photocatalytic reactions including  $\text{H}_2$  generation,  $\text{CO}_2$  reduction and degradation of persistent micropollutants [39–42]. Due to its low band gap (2.0–2.2 eV),  $\text{CdS}$  exhibits rapid recombination of charge carriers which significantly affects its photocatalytic activity. The integration of  $\text{CdS}$  with wide band gap semiconductors to prepare Z-scheme heterostructure materials has been recognized as an effective

strategy to achieve robust photocatalytic activity and enhanced separation of charge carriers [40–42]. Taking the above aspects in to consideration, in this study we have devised a simple combustion synthesis route for one pot synthesis of  $\text{Bi}_{20}\text{TiO}_{32}/\text{Bi}_4\text{Ti}_3\text{O}_{12}$  composite materials. Subsequently,  $\text{CdS}$  nanoparticles are hydrothermally deposited over the BTO/BT composite to prepare  $\text{CdS}/\text{Bi}_{20}\text{TiO}_{32}/\text{Bi}_4\text{Ti}_3\text{O}_{12}$  ternary heterostructure materials. The occurrence of a synergistic Type-I bridged coupled Z-scheme electron migration process has been ascertained from photoelectrochemical measurements, radical trapping and ESR study. The enhanced photocatalytic activity of the ternary heterostructure has been demonstrated for photodegradation of endosulfan pesticide and  $\text{H}_2$  evolution reaction under visible light irradiation.

Endosulfan (ES) is a broad-spectrum organochlorine pesticide which is extensively used in agricultural process for pest management [43]. ES isomers ( $\alpha$ - and  $\beta$ , 7:3 ratio) have been classified as persistent micro-pollutants due to their strong endocrine disrupting properties which induces carcinogenicity, reproductive damages, organ dysfunction and mutation in human being [43,44]. The long term persistency and bioaccumulation of ES in the food chain has been recognized as a vital factor for its acute toxicity in both aquatic as well as terrestrial life forms [43]. Hence, significant research efforts have been directed towards speciation/ mineralization of ES from aqueous sources. Various biotic, abiotic and light assisted processes including adsorption, biodegradation, phytoremediation, electrochemical and photochemical (UV/ $\text{H}_2\text{O}_2/\text{Fe}$ ) oxidation methods has been studied for ES removal with different degree of success [43–49]. The semiconductor photocatalytic technology offers distinct advantages in terms of use of renewable energy, economy and sustainability of the process in comparison to many conventional methods. Till date,  $\text{TiO}_2$  and  $\text{ZnO}$  based photocatalysts including  $\text{TiO}_2$  powder, N-doped  $\text{TiO}_2$ ,  $\text{TiO}_2\text{-RGO-CuFe}_2\text{O}_4$  and  $\text{ZnO-ZnS}$  has been studied for ES degradation using UV and visible radiation [50–53]. Bi-based visible light active photocatalytic materials are yet to be studied for photocatalytic degradation of endosulfan pesticide. To the best of our knowledge, this is the first report which illustrates the photocatalytic application of  $\text{CdS}/\text{Bi}_{20}\text{TiO}_{32}/\text{Bi}_4\text{Ti}_3\text{O}_{12}$  ternary photocatalyst for visible light assisted photodegradation of endosulfan.

## 2. Experimental

All chemicals (analytical reagent grade) used in this study were procured from Sigma Aldrich ltd., and Merck specialties pvt. ltd., India. Deionized water prepared in the laboratory was used in all experiments.

### 2.1. One-step combustion synthesis of $\text{Bi}_{20}\text{TiO}_{32}/\text{Bi}_4\text{Ti}_3\text{O}_{12}$ (BTC) binary heterostructure

A facile one-pot solution combustion synthesis route was devised for synthesis of the  $\text{Bi}_{20}\text{TiO}_{32}/\text{Bi}_4\text{Ti}_3\text{O}_{12}$  (BTC) material using bismuth nitrate (BN) and titanium isopropoxide (TiPO) as oxidizers and urea as fuel. In a typical procedure, BN and TiPO (6:1 molar ratio) were dissolved in 2 ml of water to make a thick paste. Required amount of urea was added to this paste and stirred further by drop wise addition of water till a clear gel is formed. The oxidizing valance of the precursors and reducing valance of the fuel was calculated using the method described by Jain et al. [54]. The fuel to oxidizer ratio in the combustion mixture was maintained at 1. The combustion gel was transferred into a furnace preheated at 400 °C and kept for 30 min. The instantaneous ignition of the combustion gel was noticed leading to the release of gaseous products. The obtained solid residue was then cooled to room temperature and grinded to make a fine powder. The combustion residue was subsequently calcined between 400 and 500 °C for 2 h to study the effect of processing temperature on the crystalline nature and phase content of the resulting material.  $\text{Bi}_{20}\text{TiO}_{32}$  being a low temperature metastable phase, the formation of  $\text{Bi}_{20}\text{TiO}_{32}/\text{Bi}_4\text{Ti}_3\text{O}_{12}$  (BTC) composite material with appreciable proportion of both components is noticed at 450 °C. The  $\text{Bi}_4\text{Ti}_3\text{O}_{12}$  material was also prepared by

combustion method by taking Bi and Ti precursors in 4:3 stoichiometric ratio and urea as fuel followed by heat treatment of the combustion residue at 600 °C for 2 h.

## 2.2. Synthesis of CdS/Bi<sub>20</sub>TiO<sub>32</sub>/Bi<sub>4</sub>Ti<sub>3</sub>O<sub>12</sub> ternary heterostructure (CdSxBTC)

The pre-synthesized BTC materials were hybridized with CdS nanoparticles using a hydrothermal synthesis route to prepare CdS/Bi<sub>20</sub>TiO<sub>32</sub>/Bi<sub>4</sub>Ti<sub>3</sub>O<sub>12</sub> ternary heterostructure materials. In a typical synthesis, required amount of cadmium nitrate was dissolved in 80 ml of deionized water followed by addition of 3 molar excess of thiourea. 500 mg of BTC powder was added to this solution and stirred for 2 h. The solution was then transferred to a 250 ml teflon lined autoclave and heated at 160 °C for 12 h. It was then cooled down to room temperature, washed 3 times with ethanol and water and dried at 60 °C for 12 h. Using above procedure, ternary composites containing 5, 10 and 20 wt% of CdS were synthesized. The ternary materials are denoted as CdSxBTC in the subsequent text, where x represents the wt% of CdS in the ternary composite. Phase pure BT and BTO were also modified with 10 wt% CdS to prepare CdS/Bi<sub>4</sub>Ti<sub>3</sub>O<sub>12</sub> (CdS10BT) and CdS/Bi<sub>20</sub>TiO<sub>32</sub> (CdS10BTO) binary heterostructure materials using similar procedure for comparative study.

## 2.3. Characterization techniques

The synthesized pure semiconductors as well as the heterostructure materials were characterized using X-ray diffraction (XRD), field emission scanning electron microscopy (FESEM), high resolution transmission electron microscopy (HRTEM), UV-Vis-DRS, photoluminescence (PL), X-ray photoelectron spectroscopy (XPS), FTIR, Raman, time resolved photoluminescence (TR-PL), transient photocurrent measurement, impedance spectroscopy, linear sweep voltammetry (LSV), Mott-Schottky and Bode phase plot analysis. The detailed methods of analysis and the analytic equipment used in the characterization study are presented in supplementary file.

## 2.4. Photocatalytic degradation of endosulfan

The photocatalytic application of the CdS/Bi<sub>20</sub>TiO<sub>32</sub>/Bi<sub>4</sub>Ti<sub>3</sub>O<sub>12</sub> ternary materials was evaluated for aqueous phase degradation of endosulfan under visible light irradiation. Initially, a 1000 ppm stock solution was prepared by dissolving the required amount of endosulfan in acetone. 1 ml of the stock solution was diluted with water to prepare a 10 ppm solution for photocatalytic study. In a typical procedure, 30 mg of the photocatalyst was dispersed in 100 ml of 10 ppm endosulfan solution by ultrasonic treatment for 10 min. To achieve the adsorption-desorption equilibrium, the solution was further stirred for 30 min under dark condition. The photodegradation process was performed in an immersion well quartz photoreactor fitted with a 250 W Xe lamp ( $\lambda > 400$  nm) under continuous stirring. The visible light intensity at the exterior surface of the reactor was measured to be 48.3 mW/cm<sup>2</sup>. The relative humidity inside the photoreactor during the reaction was 71%. At a regular time interval, 3 ml of the reaction mixture was taken out and the catalyst particles were separated by centrifugation. The concentration of endosulfan in the photodegraded solution was evaluated using HPLC [Agilent HPLC, G1322A] technique using the procedure reported in literature [55]. For HPLC analysis, acetonitrile and acidic water (acetic acid 0.1 wt%) (30:70 v/v) is used as mobile phase with a flow rate of 1.0 ml/min. The total organic carbon content at different time interval of the photocatalytic reaction was analyzed using a TOC analyzer (Analytikjena/multi N/C 3100, TOC analyzer). The chloride ions evolution was analyzed using ion selective electrodes (Orion, Thermo Scientific).

## 2.5. Photocatalytic H<sub>2</sub> generation

The photocatalytic activity of the CdSxBTC ternary composites was also evaluated for hydrogen evolution by photocatalytic water splitting using methanol as sacrificial agent. The hydrogen evolution experiment was performed in a pyrex glass photoreactor fitted with a closed gas circulation system using a 250 W xenon lamp ( $\lambda > 400$  nm) as visible light source. In a typical experiment, 100 mg of the photocatalyst was dispersed in 80 ml (10 vol%) aqueous methanol solution by stirring for 30 min. N<sub>2</sub> gas was purged continuously into the reactor for 30 min to maintain an inert environment inside the photoreactor. The suspension was then exposed to the light source and the reaction continued for 4 h. The quantitative estimation of the evolved H<sub>2</sub> gas was performed using a NUCON 5765 model GC fitted with a TCD detector. For H<sub>2</sub> generation, the conversion efficiency for hydrogen energy was calculated by using Eq. (1). The detailed calculation is presented in supplementary file.

$$\% \text{Conversion efficiency} = \frac{\text{Stored chemical energy}}{\text{Energy of incident light}} \times 100 \quad (1)$$

## 2.6. Cytotoxicity study

The cytotoxic behavior of pure endosulfan (ES), photocatalytically degraded ES solution as well as the CdS10BTC ternary photocatalyst was studied by cell viability measurement using MTT assay technique. The detail procedure for cytotoxicity study is presented in supplementary file.

## 3. Results and discussion

### 3.1. Characterization of combustion synthesized Bi<sub>20</sub>TiO<sub>32</sub>/Bi<sub>4</sub>Ti<sub>3</sub>O<sub>12</sub> (BTC) binary composite

In this study, a simple combustion synthesis route has been devised for one step synthesis of Bi<sub>20</sub>TiO<sub>32</sub>/Bi<sub>4</sub>Ti<sub>3</sub>O<sub>12</sub> composite material. The XRD patterns of the composite materials prepared at 6:1 molar ratio of the Bi:Ti salt precursors and at a F/O ratio of 1 are presented in Fig. 1I. The as obtained combustion residue shows well defined and intense XRD peaks with d-spacing values of 3.18, 2.82, 2.73, 1.95, 1.93, 1.68, 1.65 and 1.59 Å (Fig. 1Ia). These peaks are indexed to the (201), (002), (220), (222), (400), (203), (421) and (402) planes of Bi<sub>20</sub>TiO<sub>32</sub> material with a tetragonal crystal structure (JCPDS No. 42-0202). Additionally, a low intense peak observed at 3.25 Å corresponds to the (110) peak of TiO<sub>2</sub> which occurs as an impurity phase in the combustion residue. When calcined at 400 °C for 2 h, the dissolution of the impurity phase is noticed leading to the phase pure Bi<sub>20</sub>TiO<sub>32</sub> material (Fig. 1Ib).

Further heat treatment of the combustion residue at 450 °C for 2 h resulted in a mixed phase system consisting of Bi<sub>4</sub>Ti<sub>3</sub>O<sub>12</sub> and Bi<sub>20</sub>TiO<sub>32</sub> materials (Fig. 1Ic). No other analogous phases including Bi<sub>2</sub>Ti<sub>2</sub>O<sub>7</sub>, Bi<sub>2</sub>Ti<sub>4</sub>O<sub>11</sub> and Bi<sub>12</sub>Ti<sub>2</sub>O<sub>20</sub> could be detected in the XRD pattern of the binary composite. Upon calcination at 500 °C, the XRD peak due to Bi<sub>20</sub>TiO<sub>32</sub> phase decreased drastically in the composite (Fig. S1). Based on the XRD study, the composite material obtained at 450 °C is used for further study. Pure Bi<sub>4</sub>Ti<sub>3</sub>O<sub>12</sub> (BT) prepared at a calcination temperature of 600 °C displays characteristic peaks at d values of 3.75, 2.91, 2.68, 2.24, 1.88, 1.77 and 1.63 Å which are assigned to the orthorhombic phase of Bi<sub>4</sub>Ti<sub>3</sub>O<sub>12</sub> (JCPDS No. 73-2181) (Fig. 1Id). The XRD study suggests that the calcination temperature and method of synthesis are crucial for formation of the composite material. Particularly, the selective stabilization of Bi<sub>20</sub>TiO<sub>32</sub> phase which is a low temperature metastable phase has been achieved in this study using a simple combustion synthesis protocol by proper choice of reaction stoichiometry and calcination temperature.

The FESEM images of the BT, BTO and BTC materials are presented in Fig. 1II. Pure BT material exhibited pellet like particles with planar dimension of 400–600 nm and thickness 135–170 nm (Fig. 1IIC). The

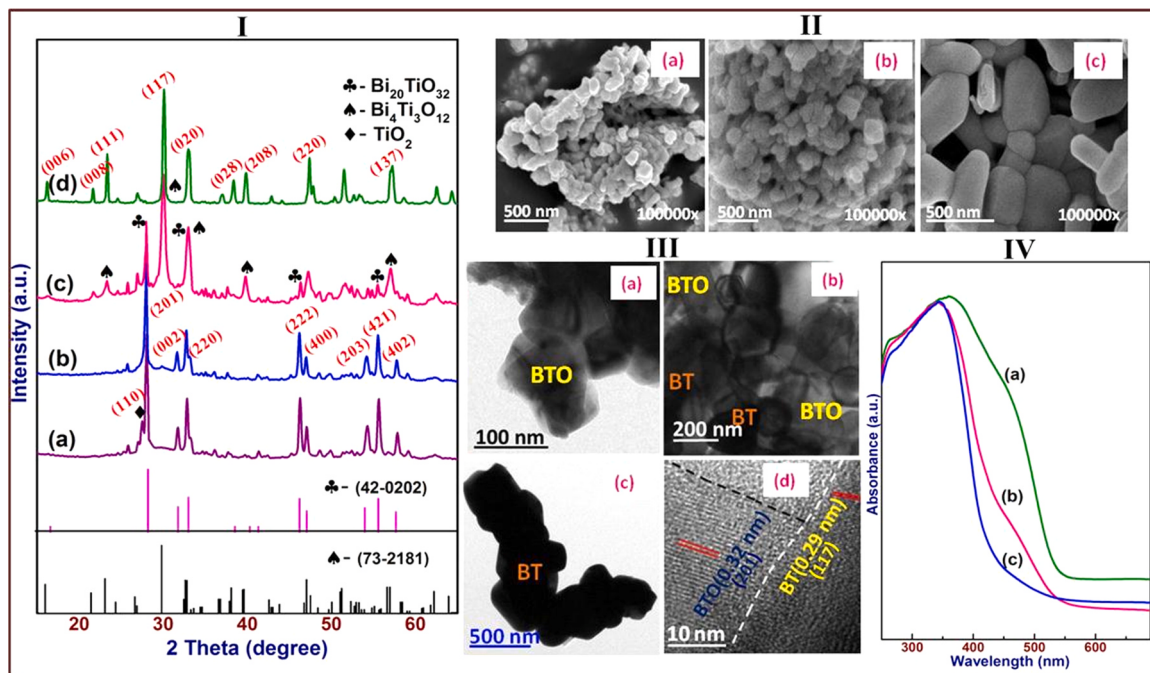


**Fig. 1.** (I) XRD patterns of (a) combustion residue and after calcination at (b) 400 °C and (c) 450 °C for 2 h, (d) BT material; (II) FESEM images of (a) BTO, (b) BTC and (c) BT materials; (III) TEM images of (a) BTO, (b) BTC, (c) BT and (d) HRTEM image of BTC material and (IV) UV-Vis spectra of a) BTO, (b) BTC and (c) BT materials.

BTO material contained submicron size two dimensional nanoparticles without any well-defined edges (Fig. 1IIa). In contrast, the BTC composite system contains agglomerated nanoparticles with size in the range of 150–300 nm (Fig. 1IIb). The apparent reduction in particle size of BT phase in the BTC can be ascribed to the lower processing temperature as well as simultaneous crystallization of both BT and BTO phases which prevent long range growth of the BT particles in the composite. The morphological features as well as the particle size of the synthesized materials are further confirmed using TEM study. The TEM image of BTO revealed the presence of plate like 2D structures with dimension 100–150 nm (Fig. 1IIIa). The BT material contains thick pellet like particle having low electron transmission property which is manifested in the form of dark images (Fig. 1IIIc). For the BTC binary composite the occurrence of two different types of particles with clear contrast is observed in the TEM study (Fig. 1IIIb). The HRTEM study revealed the merger of (201) planes of BTO and (117) planes of BT leading to the formation of the binary heterojunctions (Fig. 1IIId). The UV-Vis spectra of BT, BTO and BTC material are presented in Fig. 1IV. Pure BT material exhibits strong absorption in UV region with absorption edge occurring around 450 nm (Fig. 1IVc). The BTO material shows significant visible light absorption property with absorption edge commencing near 575 nm, which is in agreement with literature reports (Fig. 1IVa) [34,35]. The BTC composite retains the optical absorption features of both phases and shows improved optical absorption in the visible region (Fig. 1IVb). The band gap energy of pure BT and BTO material calculated from Tauc's plot are found to be 2.96 eV and 2.42 eV, respectively (Fig. S2I). Fig. S2II shows the PL spectra of BT, BTO and BTC materials acquired at an excitation wavelength of 320 nm. Both BT and BTO materials exhibit a series of PL bands in the spectral range of 400–600 nm. The prominent bands observed at 435, 460 and 560 nm can be ascribed to PL emission due to Bi<sup>3+</sup> ions ( $^3P_1 \rightarrow ^1S_0$  transition), band edge transition and presence of structural defects in the crystal lattice, respectively [56,57] (Fig. S2IIa,b). The BTC material displayed a significant suppression in the PL intensity suggesting improved separation of photogenerated charge carriers in the composite (Fig. S2IIc). The improved separation of the  $e^-/h^+$  pairs in the BTC composite can be ascribed to the formation of heterojunction between

the BT and BTO phase which facilitates the migration of charge carriers through interfacial contact (Fig. 1IIId) [58].

The microstructural property of the BTC binary composite is explored further using vibration spectroscopy. The Raman spectra of the BTC composite together with BT and BTO materials are presented in Fig. S3I. Pure BT exhibits a series of Raman bands at 852, 615, 536, 333 cm<sup>-1</sup> (A<sub>1g</sub> modes), 564, 270 cm<sup>-1</sup> (B<sub>2g</sub> modes) and 225 cm<sup>-1</sup> (B<sub>3g</sub> mode). These bands are characteristics of Bi<sub>4</sub>Ti<sub>3</sub>O<sub>12</sub> with orthorhombic crystal structure (space group Fmmm) (Fig. S3Ic) [29,59]. For tetragonal BTO material, the Raman bands are observed at 149, 225, 315, 445 and 610 cm<sup>-1</sup> (Fig. S3Ia) [60]. The vibrational Raman features of both BT and BTO materials are retained in the BTC binary composite (Fig. S3Ib). However, reduction in peak intensities as well as shift in peak positions by 5–7 cm<sup>-1</sup> is observed for both phases. Particularly, the peak intensity of the totally symmetric A<sub>1g</sub> modes of BT is significantly suppressed in the BTC composite. This observation suggests a close microscopic interaction between the BTO and BT phase which affect the symmetry of the vibration modes. The Raman study supports the formation of the BTC binary composite containing crystalline BT and BTO phases. The FTIR study further confirmed the structural integrity of both components in the composite. The composite system shows two broad vibration features at 550–650 and 800–850 cm<sup>-1</sup> corresponding to the Bi-O and Ti-O stretching vibration originating from Bi<sub>4</sub>Ti<sub>3</sub>O<sub>12</sub> as well as Bi<sub>20</sub>TiO<sub>32</sub> lattice [29,59] (Fig. S3II).

### 3.2. Characterization of the CdS/Bi<sub>20</sub>TiO<sub>32</sub>/Bi<sub>4</sub>Ti<sub>3</sub>O<sub>12</sub> (CdSxBTC) ternary composite materials

The one step combustion synthesized BTC material is used as a host lattice for construction of CdS/Bi<sub>20</sub>TiO<sub>32</sub>/Bi<sub>4</sub>Ti<sub>3</sub>O<sub>12</sub> ternary composite. The CdS phase is deposited over the BTC lattice by a facile hydrothermal route. The XRD patterns of the CdSxBTC ternary composites together with pure CdS material are presented in Fig. 2I. Pristine CdS displays characteristic diffraction peaks at d values of 3.56, 3.34, 3.14, 2.45, 2.06, 1.9, 1.76 Å which correspond to the hexagonal CdS phase (Fig. 2Ia). For CdS5BTC ternary composite the diffraction peaks due to CdS phase could not be discerned due to lower loading as well as higher

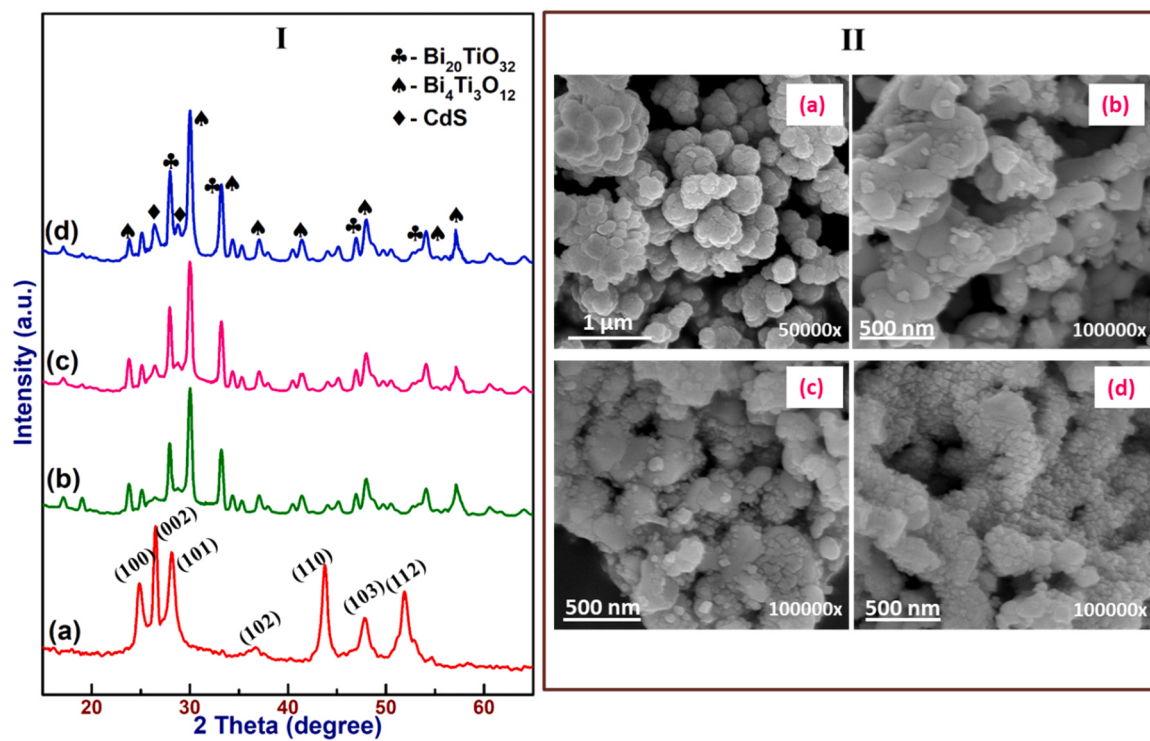


Fig. 2. (I) XRD patterns and (II) FESEM images of (a) CdS, (b) CdS5BTC, (c) CdS10BTC and (d) CdS20BTC materials.

atomic scattering factor of Bi<sup>3+</sup> ion in comparison to Cd<sup>2+</sup> ion [61] (Fig. 2Ib). However, for CdS10BTC and CdS20BTC samples the occurrence of Bi<sub>20</sub>TiO<sub>32</sub>, Bi<sub>4</sub>Ti<sub>3</sub>O<sub>12</sub> and CdS phases is clearly noted from the XRD study (Fig. 2Ic,d). The intensity of the CdS reflections at  $d$  values 3.34 and 3.14 Å are found to increase with CdS content in the hetero-structure materials. There is no apparent change in the peak position or intensity of the Bi<sub>20</sub>TiO<sub>32</sub> and Bi<sub>4</sub>Ti<sub>3</sub>O<sub>12</sub> phases in the ternary composite which suggests their structural integrity. The XRD study confirms crystalline nature of all three phases and their co-existence in the ternary composite.

The FESEM images of the ternary composites together with pure CdS are presented in Fig. 2II. Pure CdS prepared under hydrothermal condition displays presence of submicron size agglomerated spherical particles with size 200–400 nm (Fig. 2IIa). In contrast, small CdS nanoparticles uniformly distributed over the BTC lattice are clearly noticed for the ternary composites without any sign of local agglomeration (Fig. 2IId–d). The number of CdS particles per unit area increases with its content in the ternary composite. The elemental mapping images obtained from Fig. 2d reveal uniform distribution of Bi, Ti and Cd species throughout the microscopic specimen which supports the formation of the ternary composite (Fig. S4). The FESEM study confirms uniform distribution of CdS nanoparticles over BTC surface due to favorable interfacial interaction. The Bi<sub>4</sub>Ti<sub>3</sub>O<sub>12</sub> is an Aurivillius family layered perovskite oxide which contains alternating layers of fluorite like [Bi<sub>2</sub>O<sub>2</sub>]<sup>2+</sup> and perovskite-type [Bi<sub>2</sub>Ti<sub>3</sub>O<sub>10</sub>]<sup>2-</sup> slabs in its structure whereas the Bi<sub>20</sub>TiO<sub>32</sub> is isostructural with  $\beta$ -Bi<sub>2</sub>O<sub>3</sub> [30,33]. The relatively open structure of both components coupled with the intraelectric field due to charged layers of BT can facilitate adsorption of Cd<sup>2+</sup> ions on BTC surface through electrostatic and van der Waal interaction. The surface adsorbed Cd<sup>2+</sup> ions can serve as multiple nucleation sites for formation of uniformly distributed CdS nanoparticles. The TEM images of the CdS10BTC material are presented in Fig. 3. Well dispersed spherical and rectangular CdS nanoparticles with size in the range of 15–25 nm are observed in a continuous matrix of BTC composite (Fig. 3Ia–c).

The high resolution TEM images revealed the presence of three

different types of heterojunctions among BT-BTO, CdS-BTO and CdS-BT phases in the ternary composite (Fig. 3Id–f). The CdS particles are in close microscopic contact with both BTO as well as BT phases. The TEM study suggests that the ternary composite is a multi-junction hetero-structure material with large grain boundary area between the components which can help in facile migration of charge carriers. The elemental mapping images obtained from TEM study further substantiate fine dispersion of Bi, Ti, and Cd ions at microscopic level for CdS10BTC material (Fig. 3II).

The Raman spectra of CdSxBTC ternary composites together with CdS and BTC materials are presented in Fig. 4I. Pure CdS shows Raman bands at 301 cm<sup>-1</sup> and 601 cm<sup>-1</sup> which correspond to the first and second order longitudinal optical (LO) phonon modes (Fig. 4Ib) [62]. Up to 10 wt% CdS content, the Raman features of CdS could not be discerned in the ternary composite (Fig. 4Ic,d). However for 20 wt% CdS containing composite the first order LO phonon mode of CdS is observed at 298 cm<sup>-1</sup> (Fig. 4Ie). Concurrently, a gradual reduction in BTC peak intensity is also observed with CdS content due to change in microenvironment.

The UV-Vis spectra of the ternary composites together with BTC and CdS material are presented in Fig. 4II. The pristine CdS shows absorption edge near 650 nm with band gap energy of 2.2 eV (Figs. 4Ib and S2I). All the ternary composites show superior visible light absorption feature in the spectral range of 500–800 nm in comparison to the binary BTC material (Fig. 4IIC–E). The optical spectroscopy study revealed a broad spectrum response for the ternary composites material in the UV-Vis region indicating their suitability as visible light active photocatalyst. The optical band gap of the CdSxBTC ternary composites is found to be in the range of 2.1–2.7 eV (Fig. S5). The charge carrier recombination process in the CdSxBTC ternary composite is studied using photoluminescence (PL) technique. The PL spectra of CdSxBTC composite along with the BTC material are presented in Fig. 4III. The ternary composite materials exhibited significant decrease in PL intensity in comparison to the binary BTC as well as the pure components which suggests a decreased charge recombination rate in these composites (Figs. 4III and S2II).

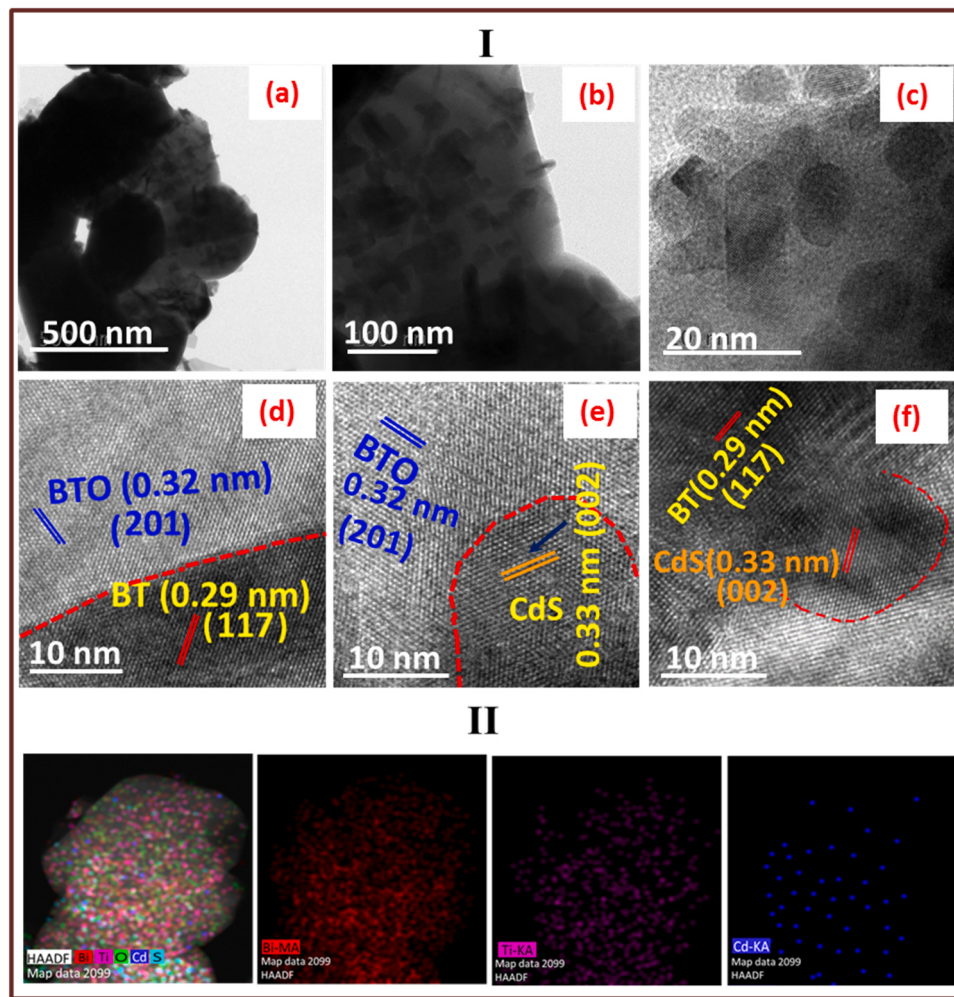


Fig. 3. (I) (a–c) TEM and (d–f) HRTEM images and (II) elemental mapping study of CdS10BTC materials.

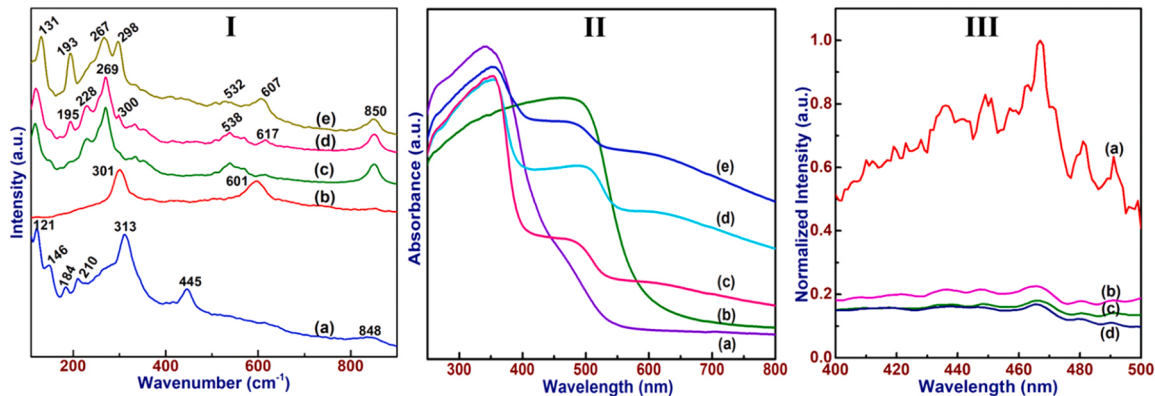
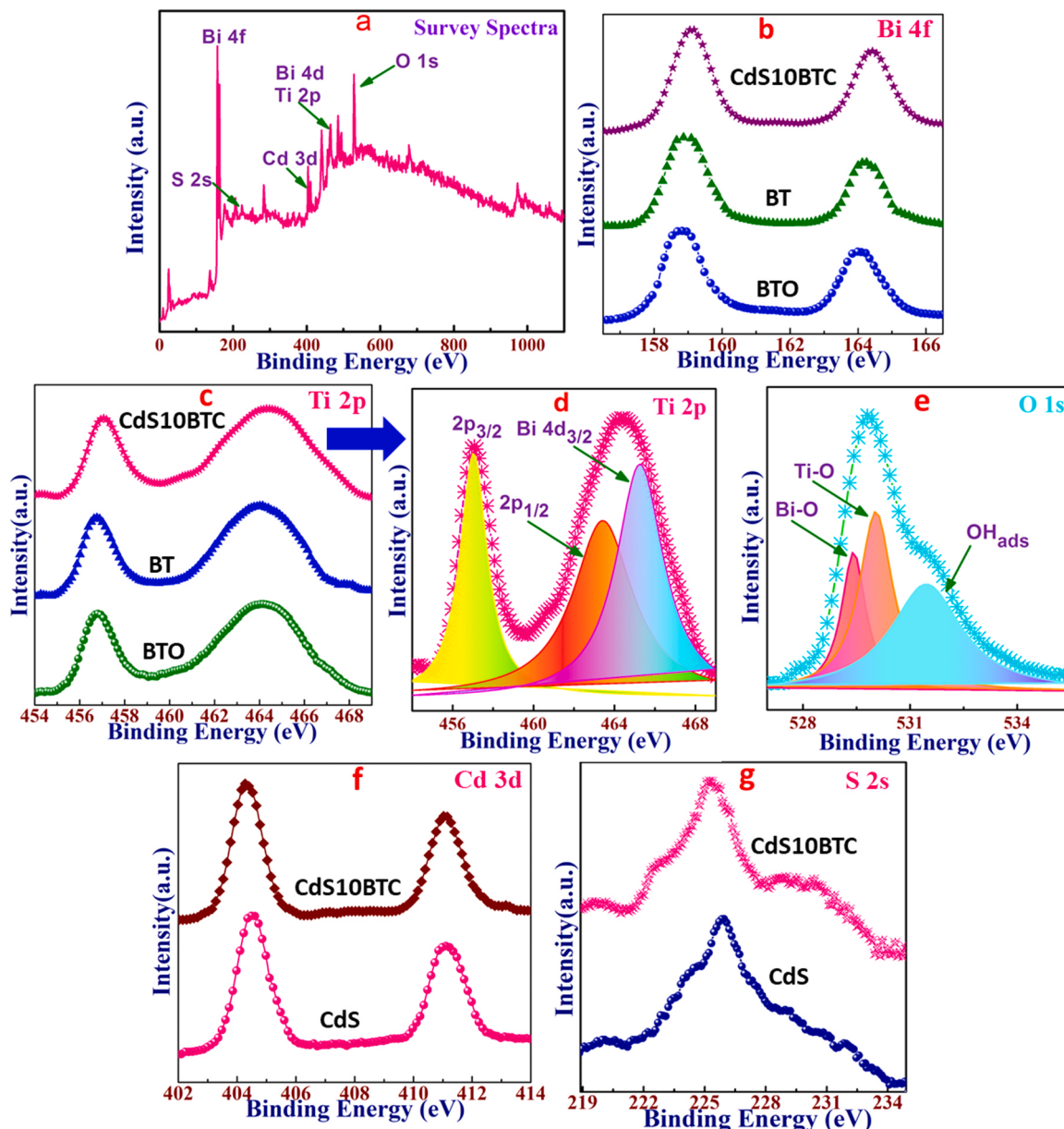


Fig. 4. (I) Raman and (II) UV-Vis spectra of (a) BTC (b) CdS (c) CdS5BTC (d) CdS10BTC (e) CdS20BTC materials and (III) Photoluminescence spectra of (a) BTC, (b) CdS5BTC, (c) CdS10BTC, (d) CdS20BTC materials.

The chemical environment and oxidation state of the elements present on the surface of the ternary composites are studied using X-ray photoelectron spectroscopy. The XPS spectra of CdS10BTC material together with pure BT, BTO and CdS are presented in Fig. 5. The survey spectrum of CdS10BTC depicts the presence of Bi, Ti, S, Cd and O together with adventitious carbon (Fig. 5a). In the Bi 4f region, a sharp and intense doublet observed at 159.1 eV and 164.3 eV corresponds to the photoelectron emission from the 4f<sub>7/2</sub> and 4f<sub>5/2</sub> microstates

(Fig. 5b). This spectral feature with spin-orbit splitting of 5.2 eV is characteristics of Bi(III) ions in an oxide environment. A comparison of the Bi4f position of CdS10BTC with the pure BT and BTO components reveal a blue shift of 0.2 eV which can be attributed to a change in the chemical microenvironment due to heterojunction formation (Fig. 5b). The high resolution spectrum of Ti in the ternary composite shows an asymmetric doublet with peak maxima at 457.1 eV and 464.4 eV (Fig. 5c). Further, the 464.4 eV peak can be de-convoluted into two



**Fig. 5.** XPS (a) survey spectra of CdS10BTC and comparison of high resolution spectra of (b) Bi 4f, (c,d) Ti 2p, (e) O 1s, (f) Cd 3d and (g) S 2s for BT, BTO, CdS and CdS10BTC materials.

peaks at 463.4 eV and 465.2 eV (Fig. 5d). The 457.1 eV peak together with 463.4 eV peak correspond to the binding energy of 2p<sub>3/2</sub> and 2p<sub>1/2</sub> energy states of Ti(IV) ions in oxide environment [29]. The 465.2 eV peak can be assigned to the Bi 4d<sub>3/2</sub> level which overlapped with Ti 2p<sub>1/2</sub> peak. The overlapping of Bi 4d<sub>3/2</sub> and Ti 2p<sub>1/2</sub> spectra has been observed earlier in the XPS study of Bi<sub>4</sub>Ti<sub>3</sub>O<sub>12</sub> and Bi<sub>12</sub>TiO<sub>20</sub> materials [63,64]. In comparison to the pure BTO and BT phase, the Ti 2p peak is shifted by 0.3 eV towards higher energy side (Fig. 5c). The O 1s region of the CdS10BTC ternary composite is quite broad and asymmetric due to presence of a variety of oxygen species in coordination with metal ions (Fig. 5e). The O 1s spectrum is fitted into three Lorentzian-resolved peaks with maxima at 529.4, 530.1 and 531.4 eV. These peaks can be assigned to lattice oxygen in coordination with Bi and Ti as well as the surface adsorbed hydroxyl group, respectively [26,65]. In the Cd 3d spectral region, a doublet is observed in the range of 403–413 eV with an intensity ratio of 5:3 for both CdS as well as CdS10BTC ternary composite (Fig. 5f). These peaks are assigned to the 3d<sub>5/2</sub> and 3d<sub>3/2</sub> energy levels of Cd(II) ions in an sulfide environment [65]. The lattice sulfur of

CdS and CdS10BTC material shows a broad peak with maxima at 225.4–225.7 eV due to photoemission from S 2s state (Fig. 5g). The S 2s peak is red shifted by 0.3 eV in the CdS10BTC ternary composite.

In this study, for the ternary composite the spectral characteristics of Bi(III) and Ti(IV) ions have shifted towards higher binding energy whereas the S(II) peak has shifted towards the lower energy side in comparison to the pure components. The XPS study implies a change in chemical environment due to interfacial interaction between the constituent phases leading to heterojunction formation.

The charge carrier separation and migration process in the composite materials are further explored using photoelectrochemical measurements. The transient photocurrent measurement of the CdS10BTC composite together with BTC and pure components are presented in Fig. S6I. The CdS10BTC ternary material exhibits significantly higher photocurrent which is nearly 3 and 2.5 times higher than pure components and BTC binary composite, respectively. The enhanced photocurrent response of CdS10BTC composite can be ascribed to improved channelization of electrons in the ternary composite. In order to examine

the long term photostability, the photocurrent measurement is carried out for CdS10BTC photocatalyst for a period of 90 min under continuous visible light irradiation. The photocurrent density quickly levels up and remains constant upto 90 min suggesting good photo-stability of the ternary photocatalyst (Fig. S6II). The electrochemical impedance spectroscopic (EIS) Nyquist plots for pure BT, BTO, CdS, binary BTC and CdS10BTC ternary material are presented in Fig. 6a. All the semiconductor materials exhibited capacitance arc in the low frequency region. The lowest semicircular arc is observed for the CdS10BTC ternary composite due to higher charge transfer ability and lower interfacial recombination rate. The Nyquist plot is fitted with an impedance circuit consisting of total ohmic resistance ( $R_1$ ), charge transfer resistance ( $R_2$ ) and constant phase element (CPE) (Fig. 6a inset). The measured charge transfer resistance ( $R_2$ ) values for BT, BTC, CdS10BTC materials are  $76.3\ \Omega$ ,  $48.2\ \Omega$  and  $35.2\ \Omega$ , respectively. The lower  $R_2$  value observed for CdS10BTC material implies less resistance to charge mobility in the ternary composite. The multi-interface structures formed between the CdS-BTO, CdS-BT and BT-BTO materials provide multiple electron transfer channels in the ternary composite thus facilitating the movement of charge carriers. Moreover, the 2D morphology of BTO and BT affords higher number of surface diffusion sites for smooth migration of charge carriers along the electrode-electrolyte interface. The above factors thus contribute to the lower charge transfer resistance of the ternary composite. For a deep understanding on the charge separation and migration process in the composite, linear sweep voltammetry (LSV) analysis is carried out. The LSV study provides useful information about the current density and charge transfer efficiency at the electrode-electrolyte interface through measurement of anodic photocurrent. In this study, all materials exhibited positive anodic photocurrent which ascertains their n-type semiconducting nature (Fig. 6b) [5]. For the pure semiconductors, anodic current value is obtained in the range of  $0.1\text{--}0.2\ \text{mA}/\text{cm}^2$  against an applied potential of  $1.5\ \text{V}$  vs. Ag/AgCl electrode.

Although the BTO and CdS materials absorb significantly in the visible region, the lower anodic photocurrent can be ascribed to the rapid recombination of the charge carriers. In contrast, the CdS10BTC composite shows superior anodic photocurrent value ( $0.42\ \text{mA}/\text{cm}^2$ )

which is nearly two times higher than pure components and 1.5 times higher than the BTC composite ( $0.27\ \text{mA}/\text{cm}^2$ ). The LSV study reveals that the heterojunction formation between CdS and BTC material stimulates higher charge transfer efficiency at the interfacial region reducing their recombination rate. The photo-electrochemical features of the ternary composites are further studied by Bode Phase plot analysis which provides vital information about resistance to charge recombination process. The Bode phase plot of the CdS10BTC material together with BTC and pure semiconductors are presented in Fig. 6c. The CdS10BTC material exhibited significant shift in the frequency maxima towards lower value which is indicative of fast electron channelization in this material due to heterojunction formation.

To explore the charge carrier separation dynamics, nanoscale time resolved photoluminescence (TR-PL) measurements are carried out to calculate average life time ( $\tau$ ) of the charge carriers. The TR-PL study is performed at an excitation wavelength of  $320\ \text{nm}$ . The fluorescence decay profiles of BTO, BTC and CdS10BTC ternary composite are presented in Fig. S6III. The curve fitting for the decay profiles is accomplished using a single exponential decay expression presented in Eq. (2) [26].

$$\frac{I(t)}{I_0} = e^{-\frac{t}{\tau}} \quad (2)$$

Where  $I(t)$ ,  $I_0$  and  $\tau$  are the photoluminescence intensity at time  $t$ , initial intensity and decay lifetime, respectively. The fluorescence life time decay ( $\tau$ ) value for CdS10BTC ( $4.14\ \text{ns}$ ) material is significantly higher than BTC ( $1.97\ \text{ns}$ ) and BTO ( $0.54\ \text{ns}$ ) materials. The prolonged life time of the charge carriers in the CdS10BTC material can be ascribed to formation of multi-heterojunctions which enhances the charge carrier migration and separation property of the composite. Mott-Schottky analysis is carried out for the pristine semiconductors to access the type of semiconductivity as well as to calculate the flat band potential ( $V_{fb}$ ). The Mott-Schottky (M-S) plots for BT, BTO and CdS materials recorded at a frequency of  $500\ \text{Hz}$  are presented in Fig. 6d-f. All three semiconductors exhibited positive slope in the M-S plot suggesting that they are n-type semiconductors. The  $V_{fb}$  value (vs Ag/AgCl) calculated

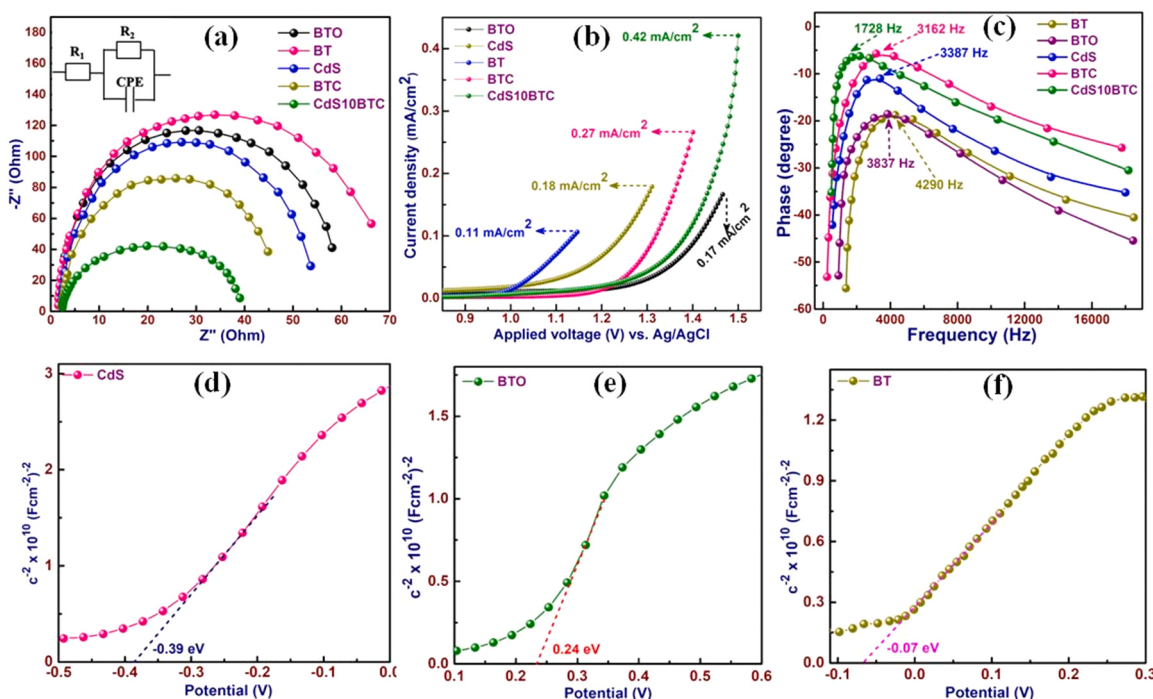


Fig. 6. (a) EIS Nyquist plots (b) Linear sweep Voltammetry and (c) Bode phase plots for BT, BTO, CdS, BTC and CdS10BTC materials and Mott-Schottky plots for (d) CdS, (e) BTO and (c) BT material.

from the intercept of the M-S plots are  $-0.39$  eV,  $0.24$  eV and  $-0.07$  eV for CdS, BTO and BT, respectively. The  $V_{fb}$  values are subsequently converted to the NHE scale using Eq. (3).

$$V_{fb(NHE, \text{pH}=7)} = V_{fb(\text{Ag/AgCl})} + 0.198 - 0.059(7 - \text{pH of the electrolyte}) \quad (3)$$

Since, conduction band minimum (CBM) of many n-type oxide semiconductors are  $0.1$ – $0.2$  eV more negative than the flat band potential, the  $V_{fb}$  values are further refined by using the method described by Ishikawa et al. [66]. The CB position of BT, BTO and CdS are found to be  $-0.02$  eV,  $0.26$  eV and  $-0.45$  eV, respectively. Using the band gap value obtained from the optical absorption study, the valence band (VB) position of the semiconductors is calculated using the expression in Eq. (4).

$$E_g = E_{VB} - E_{CB} \quad (4)$$

Where  $E_g$ ,  $E_{VB}$  and  $E_{CB}$  are the band gap energy, valance band and conduction band potential of the semiconductors. The VB potential of CdS, BTO and BT is calculated to be  $1.75$ ,  $2.68$  and  $2.94$  eV, respectively. The calculated values suggest a staggered alignment of the band

positions of the three semiconductor components in the composite which is conducive for fast electron channelization.

### 3.3. Photocatalytic activity

#### 3.3.1. Photocatalytic degradation of endosulfan

The photocatalytic application of the CdSxBTC ternary composite is studied for degradation of endosulfan pesticide from aqueous phase under visible light irradiation. Initially, in order to ascertain the photocatalytic nature of the degradation reaction, experiments are carried out under dark and illuminated condition in presence and absence of the CdSxBTC photocatalysts. Under dark condition, the degradation reaction does not occur in absence or present of the CdSxBTC photocatalysts. Under illuminated condition, in absence of the photocatalysts no substantial degradation is noted due to the persistent nature of endosulfan [43]. The photocatalytic activity of the ternary composites is compared with the pure components as well as the binary BTC material in Fig. 7I. Although the pure semiconductors are active, the degradation reaction is quite sluggish achieving  $20$ – $30\%$  photodegradation efficiency (PDE) after  $90$  min of irradiation time (Table 1). The low activity observed for the pure semiconductors can be ascribed to the higher rate of charge

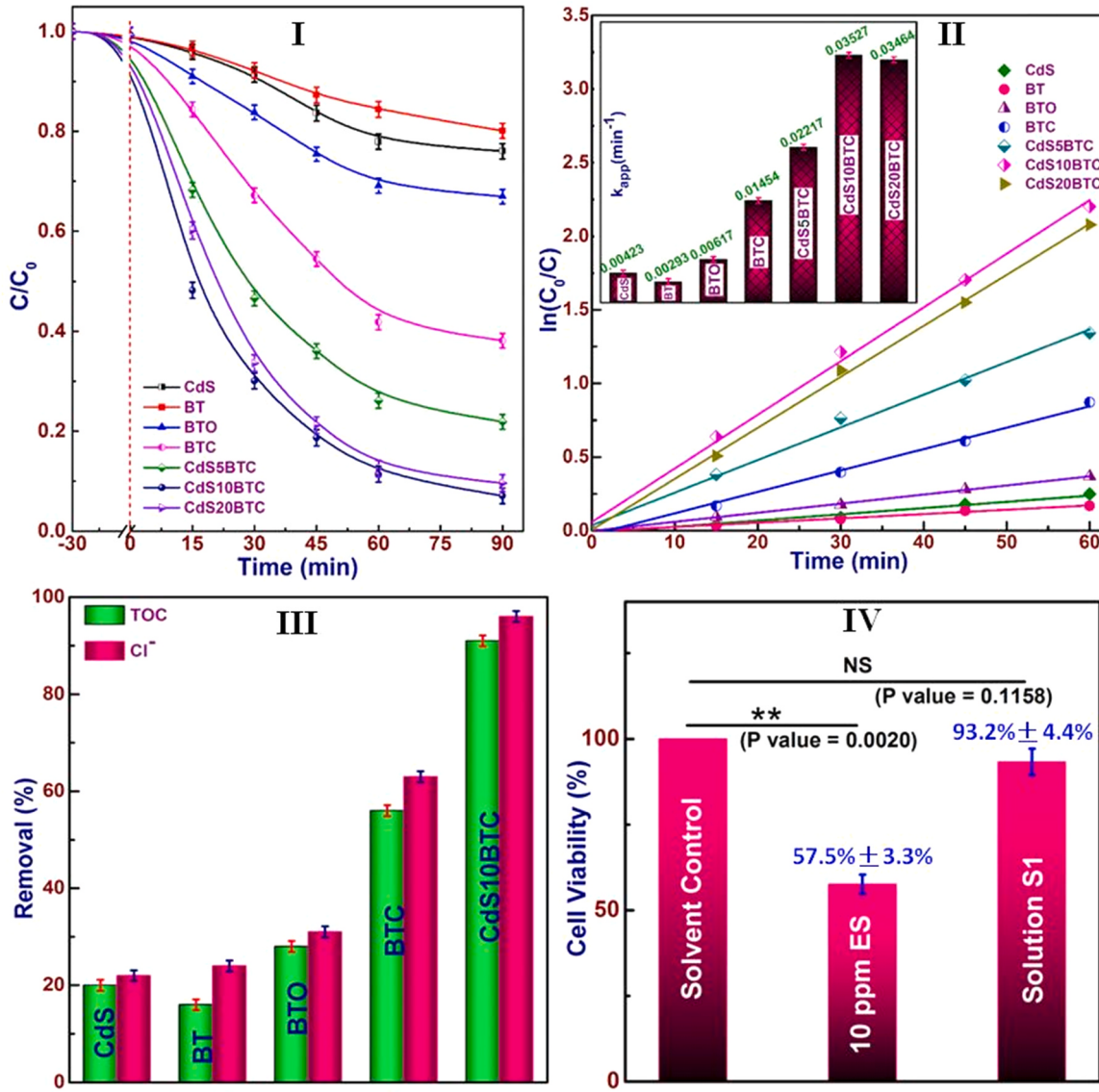


Fig. 7. (I) Photocatalytic degradation of endosulfan; (II) pseudo first order kinetics plots and (III) TOC and  $\text{Cl}^-$  ion removal after 90 min for BT, BTO, CdS, BTC and CdSxBTC materials and (IV) Cytotoxicity study of 10 ppm parent ES solution before and after photocatalytic treatment.

**Table 1**

Photodegradation efficiency (PDE) and kinetics data for degradation of ES over CdSxBTC ternary photocatalysts.

Catalyst	$K_{app}$ (min <sup>-1</sup> )	R <sup>2</sup>	Standard error <sup>a</sup>	PDE (%)
CdS	0.00423	0.98275	0.00035	23.9
BT	0.00293	0.99192	0.00013	19.8
BTO	0.00617	0.99855	0.00011	33.0
BTC	0.01454	0.99332	0.00059	61.8
CdS10BTO	0.01586	0.98862	0.00101	70.6
CdS10BT	0.01621	0.99327	0.00116	72.7
CdS5BTC	0.02217	0.99264	0.00095	78.0
CdS10BTC	0.03527	0.99532	0.00125	92.9
CdS20BTC	0.03464	0.99869	0.00062	90.3

(Experimental condition: 30 mg catalyst, 100 ml of 10 ppm ES solution, reaction time 90 min, 250 W Xe lamp).

<sup>a</sup> Standard error values for the slope of the pseudo 1st order kinetics equation.

carrier recombination. The binary BTC composite exhibits improved activity in comparison to the pure components achieving 61.8% PDE. However, when CdS is integrated with BTC, a substantial improvement in the % PDE is observed. The CdSxBTC ternary composites exhibited PDE in the range of 78–93% with the best result of 92.9% PDE is observed for the CdS10BTC composite (Table 1). In order to access the role of each semiconductor components in the composite, the CdS10BT and CdS10BTO composite materials are also prepared and studied for ES degradation (Fig. S7). The CdS10BTC composite exhibited significantly higher activity than the binary composites due to synergistic action of all three components in the composite. The improved PDE of the ternary composites can be ascribed to multi-heterojunction formation which results in efficient space separation of the charge carriers. The degradation curves are fitted into pseudo first order kinetics model with correlation coefficient (R<sup>2</sup>) > -98% using the expression presented in Eq. (5).

$$\ln \frac{C_0}{C} = k_{app} t \quad (5)$$

Where C<sub>0</sub> and C are the initial ES concentration and at time t min and k<sub>app</sub> is the pseudo-first order rate constant in min<sup>-1</sup>. The k<sub>app</sub> values calculated from the slope of the ln(C<sub>0</sub>/C) vs t plots (Fig. 7II) for different photocatalysts are presented in Table 1. The CdS10BTC photocatalyst exhibited K<sub>app</sub> value of  $3.52 \times 10^{-2}$  min<sup>-1</sup> which is nearly 12, 6 and 2.5 times higher than BT, BTO and BTC composite materials.

The ES degradation activity is further monitored by total organic carbon (TOC) analysis as well as estimation of evolved Cl<sup>-</sup> ions after 90 min of reaction time (Fig. 7III). The CdS10BTC photocatalyst exhibits substantially higher TOC removal and release of free Cl<sup>-</sup> ions compared to the pure components as well the BTC binary composite. After 90 min of irradiation, 91% reduction in TOC and 96% release of Cl<sup>-</sup> ions are observed for CdS10BTC material. The TOC study implies that a small portion of degradation intermediates still occur as persistent organic impurity which could not be mineralized further over the CdS10BTC photocatalyst surface.

The degradation reaction protocol is optimized by varying the catalyst amount and ES concentration in the reaction mixture by taking the optimal CdS10BTC ternary composite as photocatalyst (Fig. S8). The optimization study suggested that 300 mg L<sup>-1</sup> photocatalyst can be efficiently used for degradation of up to 10 ppm ES solution with > 90% efficiency. In order to access the application potential of the developed photocatalytic protocol, photodegradation of ES is carried out in different water matrices as well as in presence of interfering anions with radical scavenging properties (Fig. S9). A moderate reduction of 10–15% in photocatalytic activity is observed in presence of monovalent and divalent anions probably due to competitive chemisorption as well as radical scavenging property (Fig. S9I). Particularly, the decrease is more prominent for PO<sub>4</sub><sup>3-</sup> ions which show strong •OH radical scavenging property (Fig. S9I). Among different point sources, the

photocatalytic activity is significantly attenuated in agricultural runoff and municipality water (Fig. S9II). For these water matrices, 74% and 78% of endosulfan degradation activity is observed over CdS10BTC photocatalyst, respectively. The apparent decrease in photocatalytic activity can be ascribed to different factors including reduced dissolved oxygen (DO), presence of suspended solid as well as other radical scavengers in these water samples. Nevertheless, the CdS10BTC catalyzed photocatalytic protocol shows satisfactory response for ES degradation in different water matrices indicating its suitability for practical application.

The cytotoxic property of the water sample after photocatalytic treatment is an important parameter to access its suitability for subsequent use. The cytotoxicity of the treated ES solution is studied by MTT assay technique by employing human leukemia monocyte (THP1) cell lines as substrate. Initially, the MTT experiments are optimized by taking different amount (1–6 µL) of photocatalytically treated ES solution. Up to a volume of 5 µL, no appreciable decrease in cell viability is noticed (Fig. S10I). Based on this observation, the cell viability study of the parent ES solution is performed by taking 5 µL sample. The cell viability of 10 ppm endosulfan solution is compared with photocatalytically treated ES sample in Fig. 7IV. The parent ES solution shows a 43% loss in cell viability after an incubation period of 72 h which substantiates its toxic nature. In comparison, the photocatalytically treated solution shows higher cell viability (93%) due to effective mineralization of endosulfan to innocuous products. The significance (p) values calculated by paired t-test method suggest that the cell viability is statistically significant for parent ES solution (0.0020) whereas it is statistically non-significant (0.1158) for the treated solution in comparison to the control group. In addition, the CdS10BTC ternary photocatalyst is also found to show > 90% cell viability up to a concentration of 500 mg/L which suggest its non-cytotoxic nature (Fig. S10II).

The recyclability of a photocatalyst is an important aspect for its practical application. In this study, the recyclability of CdS10BTC photocatalyst is studied for five consecutive cycles for ES degradation reaction. After every cycle, the catalyst particles are generated by multiple washing with acetone and then drying in an oven at 80 °C for 6 h. The CdS10BTC photocatalyst exhibited stable photocatalytic activity with a minimal decrease of 4% activity after fifth catalytic cycle (Fig. S11). The XRD patterns and FESEM images of CdS10BTC photocatalyst before and after the photocatalytic study are presented in Fig. S11(II and III). The crystalline character, phase content and morphology of CdS10BTC composite remain intact after fifth photocatalytic cycle. In order to further confirm the stability of the ternary composite, the photodegraded ES solution after 90 min of reaction time is analyzed for Cd<sup>2+</sup> ions by atomic absorption spectroscopy. No appreciable concentration of leached Cd<sup>2+</sup> could be detected in the experimental solution which suggests excellent stability of the ternary composite during ES photodegradation.

### 3.3.2. Photocatalytic hydrogen production

The photocatalytic application of the pure components, BTC binary and CdSxBTC ternary composite materials is further explored for hydrogen production by photocatalytic water splitting. The H<sub>2</sub> evolution reactions are carried out using methanol as a sacrificial agent to capture photogenerated holes. The H<sub>2</sub> evolution rate for the CdSxBTC photocatalysts is compared with CdS, BT, BTO and BTC materials in Fig. 8. Pure BTO is inactive for H<sub>2</sub> evolution reaction due to insufficient reduction potential (CBM at 0.26 eV) of the CB electrons. For BT and CdS, the hydrogen evolution rates are 40 µmol g<sup>-1</sup> h<sup>-1</sup> and 150 µmol g<sup>-1</sup> h<sup>-1</sup>, respectively which suggest slow nature of the reaction (Fig. 8I). Although, both these pristine semiconductors possess required CB potential (CBM of BT and CdS is -0.02 and -0.45 eV, respectively), the rapid recombination of charge carriers is responsible for the lower rate of H<sub>2</sub> evolution. In contrast, the CdSxBTC materials exhibited improved H<sub>2</sub> evolution activity with maximum H<sub>2</sub> evolution rate of

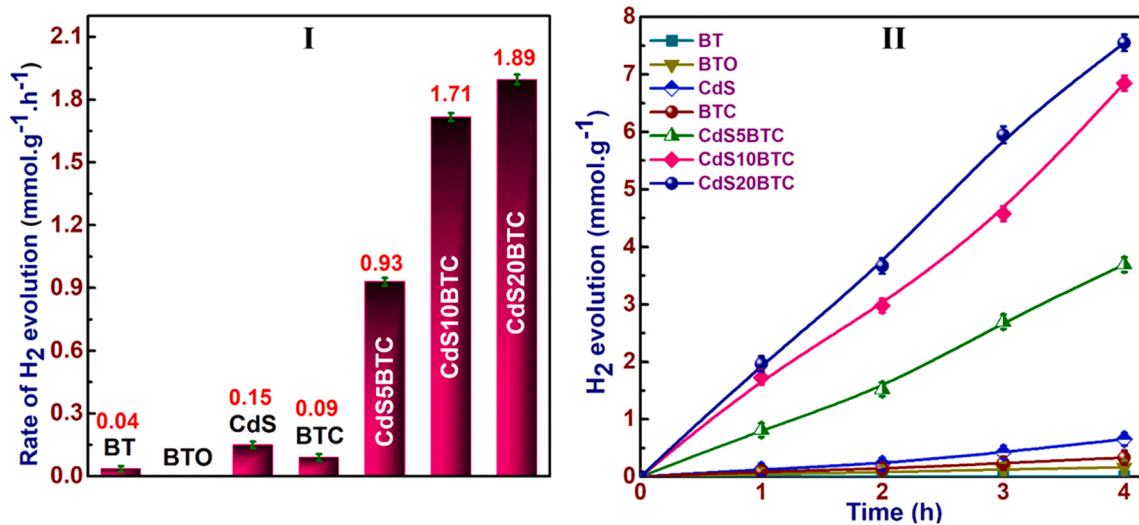


**Fig. 8.** (I) Photocatalytic H<sub>2</sub> evolution rate and (b) H<sub>2</sub> evolution wrt different irradiation time for the pure semiconductors (BT, BTO, CdS), BTC and CdSxBTC composite materials.

1890  $\mu\text{mol g}^{-1}\text{h}^{-1}$  observed for CdS20BTC composite material. The H<sub>2</sub> evolution rate of CdS20BTC material is nearly 45 and 12 times higher than pristine BTO and CdS and 20 times higher than the BTC binary composite material. The apparent conversion efficiency of the CdS20BTC photocatalyst is found to be 19% (detailed calculation presented in supplementary file). The H<sub>2</sub> evolution activity of CdS20BTC photocatalyst is also studied in different water matrices (Fig. S12). A minimal decrease of 5% in photocatalytic activity is noticed which suggest that the CdS20BTC photocatalyst can be used for H<sub>2</sub> generation from different water matrices. The recyclability of the CdS20BTC photocatalyst is studied for three consecutive cycles (Fig. S13). A marginal loss of 3% in photocatalytic activity is noticed after the third cycle. The crystalline nature and morphology of the regenerated CdS20BTC photocatalyst remain unaltered suggesting good stability of the ternary photocatalyst for H<sub>2</sub> evolution reaction (Fig. S13II and III).

### 3.3.3. Photocatalytic mechanism

In order to identify the active species involved in the photo-degradation of ES, photocatalytic experiments are conducted in presence of different radical scavengers. Ammonium oxalate, AgNO<sub>3</sub>, benzoquinone and tertiary butyl alcohol are employed as scavengers for h<sup>+</sup>, e<sup>-</sup>, O<sub>2</sub><sup>-</sup> and OH radicals, respectively. Significant reduction of ES

degradation rate is observed in presence of O<sub>2</sub><sup>-</sup> and OH radical scavengers (Fig. S14). A moderate decrease in reaction rate is also noticed for h<sup>+</sup> scavenger. The scavenger experiments suggest that the O<sub>2</sub><sup>-</sup> and OH radicals are the primary species responsible for photodegradation of endosulfan. The in situ generation of these reactive species in the aqueous illuminated suspension of the CdSxBTC ternary photocatalyst is further confirmed by spectroscopic method using nitroblue tetrazolium chloride (NBT) and terephthalic acid (TA) as probe molecules. The detailed procedures for these experiments are presented in supplementary file. Terephthalic acid rapidly consumes OH radicals to form fluorescent 2-hydroxy terephthalic acid (HTA) which shows a PL emission maxima at 425 nm. The appearance of this PL band and its gradual increase in intensity can be quantitatively correlated to the amount of OH radicals generated in the catalyst aqueous suspension [25,67]. The PL spectra of HTA formed in the aqueous suspension of pristine BT, binary composites (BTC, CdS10BT, CdS10BTO) and CdS10BTC ternary photocatalysts are presented in Fig. S15. The increase in PL intensity with irradiation time for these materials is also shown in Fig. 9I. Among the pure components, BT and BTO are capable of generating OH radicals in aqueous suspension. The valance band maximum (VBM) of these materials possesses sufficient positive potential to carry out OH/OH (1.99 eV vs NHE) and H<sub>2</sub>O/OH (+ 2.27 eV vs NHE) oxidation [9,14]

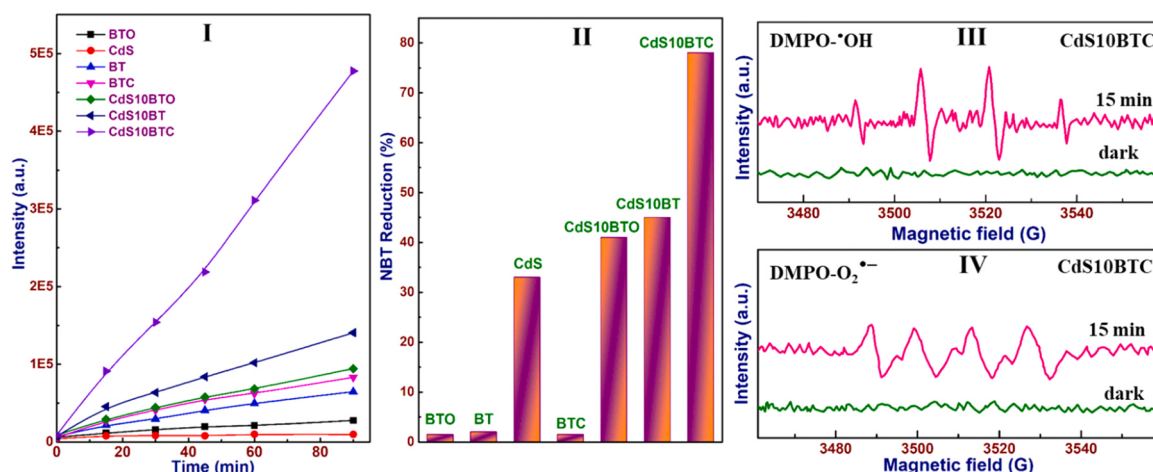


**Fig. 9.** (I) Comparison of PL intensities of HTA and (II) Percentage NBT reduction in aqueous suspension of different photocatalyst (III & IV) ESR spectra of DMPO-OH and DMPO-O<sub>2</sub><sup>-</sup> adduct in aqueous suspension of CdS10BTC under dark and illuminated conditions.

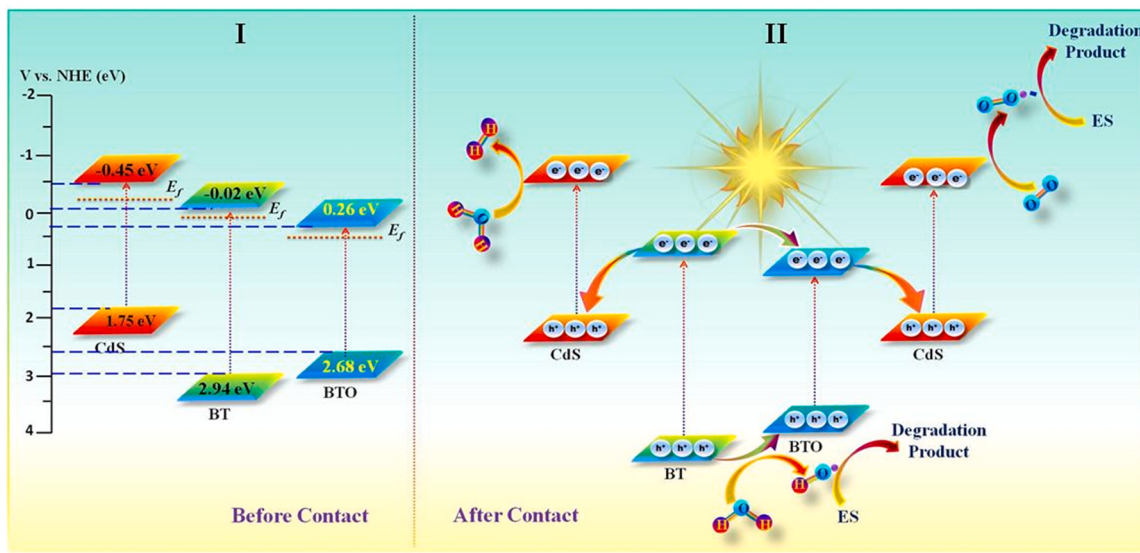


**Fig. 10.** Plausible mechanism for photo-degradation of endosulfan over the CdS10BTC photocatalyst surface.

(Fig. 10I). Among the composites, the CdS10BTC material exhibits rapid increase in HTA PL intensity with time which suggests expeditious formation of  $\cdot\text{OH}$  radicals for this ternary photocatalyst (Fig. 9I). After 90 min of irradiation, the PL intensity of CdS10BTC photocatalyst is approximately 5 times higher than BTC and CdS10BTO and 3.5 times higher than the CdS10BT binary composites. The  $\cdot\text{OH}$  radical generation ability of CdS10BTC photocatalyst is further confirmed from ESR study using DMPO as spin trapping agent (Fig. 9III). The experimental procedure for spin trapping study using ESR technique is presented in supplementary file. The characteristic spectral features of DMPO- $\cdot\text{OH}$  adduct are clearly noticed in ESR study under illuminated condition which confirm  $\cdot\text{OH}$  radical formation [25,26].

A quantitative assessment of  $\cdot\text{O}_2^-$  radical generation ability of different photocatalysts is carried out using NBT as molecular probe. In aqueous media, NBT reacts with superoxide radicals in a stoichiometric ratio of 1:4 to form purple formazan derivative [67,68]. The molecular absorption peak of NBT at  $\lambda = 280$  nm is thus rapidly attenuated in a catalyst suspension upon formation of  $\cdot\text{O}_2^-$  radicals. The UV-Vis spectra of NBT in presence of different photocatalysts as a function of irradiation time are presented in Fig. S16. A comparison of percentage decrease in NBT peak intensity after 90 min of irradiation is also presented in Fig. 9II. For BT, BTO and BTC photocatalysts no appreciable reduction in NBT peak intensity could be noticed upto 90 min of irradiation. These semiconductors are incapable of dioxygen reduction due to insufficient potential of the conduction band electrons ( $\text{O}_2/\text{O}_2^- = -0.33$  eV) [9, 18]. On the other hand, significant decrease in NBT peak intensity is observed for pure CdS and CdS containing binary and ternary composites (Fig. 9II). Highest NBT transformation rate is observed for CdS10BTC photocatalyst which is nearly 2.5 and 1.5 times higher than pure CdS and CdS based binary composites (CdS10BT and CdS10BTO). The in situ formation of  $\cdot\text{O}_2^-$  radical is further confirmed from ESR spin trapping study using DMPO as probe molecule. The ESR spectra of a methanolic suspension of CdS10BTC photocatalyst under dark condition and after 15 min of illumination is presented in Fig. 9IV. Under illuminated condition, the appearance of ESR signal due to the DMPO- $\cdot\text{O}_2^-$  spin adduct confirms the formation of the  $\cdot\text{O}_2^-$  radicals [25].

The radical trapping study suggests robust generation of  $\cdot\text{OH}$  and  $\cdot\text{O}_2^-$  radicals in the aqueous suspension of the CdSxBTC ternary photocatalyst due to heterojunction formation between the constituent phases. Moreover, the radical generating ability of the ternary composite is much higher than the BTC, CdS10BT and CdS10BTO binary photocatalysts. The synergistic action of all three component semiconductors seems to be a crucial factor for efficient channelization and

space separation of electron-hole pairs in the ternary composite. In order to adequately explain the formation of radical species and observed photocatalytic activity, a plausible electron migration scheme is proposed for the ternary composite photocatalyst in Fig. 10. All the three components (BT, BTO and CdS) in the composite possess appropriate band gap energy to absorb visible light photons and undergo photo-excitation (Fig. 10I). Due to favorable band alignment of BT and BTO with CdS, the photoelectrons from the CB of BT and BTO can migrate and recombine with the VB  $\text{h}^+$  of CdS forming Z-scheme heterojunctions (Fig. 10II). Such electron migration is driven by three factors, namely (1) staggered nature of band alignment, (2) energy proximity between the CB of BT & BTO with - VB of CdS and (3) the electrostatic attraction between  $\text{e}^-$ - $\text{h}^+$  pairs. In addition, the band structure of BT and BTO is suitable for formation of a Type-I heterojunction where the charge carriers can migrate from the BT to BTO. The proposed electron migration scheme is consistent with the TEM observations where three distinct types of heterojunctions have been noticed between BT-BTO, BTO-CdS and BT-CdS phases.

The coupled Z-scheme electron migration mechanism presented in Fig. 10II also accounts for the higher photostability of the ternary composite. The rapid neutralization of  $\text{h}^+$  species in the VB of CdS prevents the photobleaching of  $\text{Cd}^{2+}$  ions thereby increasing the photostability of the composite [69]. Under the proposed electron migration scheme, the photoelectrons resides in the CB of CdS with sufficiently 've' potential (-0.45 eV) to carry out dioxygen reduction to  $\cdot\text{O}_2^-$  radicals. Moreover, the  $\text{h}^+$  population present in the VB of BT (+2.94 eV) & BTO (+2.68 eV) can oxidize  $\text{H}_2\text{O}/\text{OH}^-$  to  $\cdot\text{OH}$  radical by virtue of their high positive potential. The coupled Z-scheme mechanism is thus consistent with the observations from radical trapping study and support the rapid formation of  $\cdot\text{OH}$  and  $\cdot\text{O}_2^-$  radicals in the ternary composite. The radical mechanism for photodegradation of ES and hydrogen evolution reaction is presented in Eqs. (6)–(17).

#### Endosulfan oxidation



ES+•OH→oxidation products	(10)
HO <sub>2</sub> •+H <sub>2</sub> O→H <sub>2</sub> O <sub>2</sub> +•OH	(11)
H <sub>2</sub> O <sub>2</sub> +•O <sub>2</sub> →OH <sup>-</sup> +•OH+O <sub>2</sub>	(12)
OH <sup>-</sup> +h <sup>+</sup> →•OH	(13)
ES+•O <sub>2</sub> →oxidation products	(14)
ES+h <sup>+</sup> →oxidation products	(15)
<i>Hydrogen evolution</i>	
2 H <sub>2</sub> O+4 h <sup>+</sup> →O <sub>2</sub> (g)+4 H <sup>+</sup>	(16)
2 H <sup>+</sup> +2e <sup>-</sup> →H <sub>2</sub> (g)	(17)

#### 4. Conclusion

The synthesis and visible light assisted photocatalytic application of a new ternary CdS/Bi<sub>20</sub>TiO<sub>32</sub>/Bi<sub>4</sub>Ti<sub>3</sub>O<sub>12</sub> multi-heterojunction photocatalyst has been reported in this work for expeditious photodegradation of endosulfan and hydrogen evolution reaction. Combustion synthesis method is employed as a simple and less time consuming method for facile synthesis of Bi<sub>20</sub>TiO<sub>32</sub>/Bi<sub>4</sub>Ti<sub>3</sub>O<sub>12</sub> the binary composite. The hydrothermal synthesis of CdS over the binary composite resulted in fine dispersion of CdS nanoparticles (15–25 nm) over a continuous BTC matrix. The presence of crystalline hexagonal CdS, tetragonal Bi<sub>20</sub>TiO<sub>32</sub> and orthorhombic Bi<sub>4</sub>Ti<sub>3</sub>O<sub>12</sub> has been confirmed from structural study. Morphological investigation suggested formation of three different types of heterojunctions through nanosized interfacial contact among the semiconductor components in the ternary composite. The ternary heterojunctions displayed improved optical absorption and photoelectrochemical features including less resistance to charge mobility, enhanced transient photocurrent response, rapid migration of charge carrier and higher excited state lifetime. The CdSxBTC ternary photocatalyst showed excellent photocatalytic activity for endosulfan degradation (> 92%) and hydrogen evolution reaction (1890 μmolg<sup>-1</sup>h<sup>-1</sup>) which is nearly a magnitude higher than the pure bismuth titanate semiconductors. Cytotoxicity study suggested higher cell viability for photodegraded endosulfan solution. The ternary composite demonstrated expeditious generation of •OH and •O<sub>2</sub><sup>-</sup> radicals under illuminated condition. A synergistic electron migration scheme involving a Type-I bridged coupled Z-scheme system has been proposed to account for the observed photophysical and photocatalytic property of the ternary composite.

#### CRediT authorship contribution statement

**Krishnendu Das:** Preparation of the ternary composites and photocatalytic application study, manuscript writing, Conceptualization, Methodology. **Ranjit Bariki:** Characterization study using XRD, Raman and interpretation of data. **Dibyananda Majhi:** XPS and microscopic study. **Abtar Mishra and Rohan Dhiman:** Cytotoxicity study. **Kundan K. Das:** Data curation, interpretation. **B.G. Mishra:** Supervision, Conceptualization, Methodology, Funding acquisition, Writing – review & editing.

#### Declaration of Competing Interest

The authors declare that they have no known competing financial interests or personal relationships that could have appeared to influence

the work reported in this paper.

#### Acknowledgment

We would like to thank Council of Scientific and Industrial Research (CSIR), New Delhi, India for financial support (Grant 01(2947)/18/EMR-II). We would also like to thank DST-FIST, New Delhi for infrastructural grant (SR/FTP/CS-I/2010/18).

#### Appendix A. Supporting information

Supplementary data associated with this article can be found in the online version at doi:10.1016/j.apcatb.2021.120902.

#### References

- [1] H. Li, Y. Zhou, W. Tu, J. Ye, Z. Zou, State-of-the-art progress in diverse heterostructured photocatalysts toward promoting photocatalytic performance, *Adv. Funct. Mater.* 25 (2015) 998–1013.
- [2] K. Wang, Z. Xing, M. Du, S. Zhang, Z. Li, K. Pan, W. Zhou, Hollow MoSe<sub>2</sub>@Bi<sub>2</sub>S<sub>3</sub>/CdS core-shell nanostructure as dual Z-scheme heterojunctions with enhanced full spectrum photocatalytic-photothermal performance, *Appl. Catal. B Environ.* 281 (2021), 119482.
- [3] J. Luo, S. Zhang, M. Sun, L. Yang, S. Luo, J.C. Crittenden, A critical review on energy conversion and environmental remediation of photocatalysts with remodeling crystal lattice, surface, and interface, *ACS Nano* 13 (2019) 9811–9840.
- [4] G. Zhang, Z. Wang, J. Wu, Construction of a Z-scheme heterojunction for high-efficiency visible-light-driven photocatalytic CO<sub>2</sub> reduction, *Nanoscale* 13 (2021) 4359–4389.
- [5] R. Bariki, D. Majhi, K. Das, A. Behera, B.G. Mishra, Facile synthesis and photocatalytic efficacy of UIO-66/CdIn<sub>2</sub>S<sub>4</sub> nanocomposites with flowerlike 3D-microspheres towards aqueous phase decontamination of triclosan and H<sub>2</sub> evolution, *Appl. Catal. B Environ.* 270 (2020), 118882.
- [6] R. Marschall, Semiconductor composites: strategies for enhancing charge carrier separation to improve photocatalytic activity, *Adv. Funct. Mater.* 24 (2014) 2421–2440.
- [7] Z. Gao, J. Wang, Y. Muhammad, Y. Zhang, S.J. Shah, Y. Hu, Z. Chu, Z. Zhao, Z. Zhao, Enhanced moisture-resistance and excellent photocatalytic performance of synchronous N/Zn-decorated MIL-125(Ti) for vaporous acetaldehyde degradation, *Chem. Eng. J.* 388 (2020), 124389.
- [8] P. Hu, R. Wang, Z. Gao, S. Jiang, Z. Zhao, H. Ji, Z. Zhao, Improved interface compatibility of hollow H-Zr<sub>0.1</sub>Ti<sub>0.9</sub>O<sub>2</sub> with UiO-66-NH<sub>2</sub> via Zr-Ti bidirectional penetration to boost visible photocatalytic activity for acetaldehyde degradation under high humidity, *Appl. Catal. B: Environ.* 296 (2021), 120371.
- [9] Z. Zhang, Y. Muhammad, Y. Chen, S.J. Shah, Y. Peng, S. Shao, R. Wang, X. Li, H. Liu, Z. Zhao, Construction of ultra-stable and Z-scheme Fe-Graphdiyne/MIL-100 (Fe) photo-Fenton catalyst with C = C—Fe—O interface for the highly enhanced catalytic degradation of Dinoflagellate, *Chem. Eng. J.* 426 (2021), 131621.
- [10] H. He, Y. Wang, J. Li, S. Jiang, S. Sidra, W. Gong, Y. Tang, Y. Hu, R. Wei, D. Yang, X. Li, Z. Zhao, Confined conductive and light-adsorbed network in metal organic frameworks (MIL-88B(Fe)) with enhanced photo-Fenton catalytic activity for sulfamethoxazole degradation, *Chem. Eng. J.* 427 (2022), 131962.
- [11] C. Liu, J. Xu, J. Niu, M. Chen, Y. Zhou, Direct Z-scheme Ag<sub>3</sub>PO<sub>4</sub>/Bi<sub>4</sub>Ti<sub>3</sub>O<sub>12</sub> heterojunction with enhanced photocatalytic performance for sulfamethoxazole degradation, *Sep. Purif. Technol.* 241 (2020), 116622.
- [12] D. Majhi, A.K. Mishra, K. Das, R. Bariki, B.G. Mishra, Plasmonic Ag nanoparticle decorated Bi<sub>2</sub>O<sub>3</sub>/CuBi<sub>2</sub>O<sub>4</sub> photocatalyst for expeditious degradation of 17α-ethynodiol and Cr(VI) reduction: Insight into electron transfer mechanism and enhanced photocatalytic activity, *Chem. Eng. J.* 413 (2021), 127506.
- [13] F. He, B. Zhu, B. Cheng, J. Yu, W. Ho, W. Macay, 2D/2D/OD TiO<sub>2</sub>/C<sub>3</sub>N<sub>4</sub>/Ti<sub>3</sub>C<sub>2</sub> MXene composite S-scheme photocatalyst with enhanced CO<sub>2</sub> reduction activity, *Appl. Catal. B Environ.* 272 (2020), 119006.
- [14] A. Kumar, G. Sharma, A. Kumari, C. Guo, M. Naushad, D.V.N. Vo, J. Iqbal, F. J. Stadlera, Construction of dual Z-scheme g-C<sub>3</sub>N<sub>4</sub>/Bi<sub>4</sub>Ti<sub>3</sub>O<sub>12</sub>/Bi<sub>4</sub>O<sub>5</sub>I<sub>2</sub> heterojunction for visible and solar powered coupled photocatalytic antibiotic degradation and hydrogen production: Boosting via I<sup>-</sup>/I<sub>3</sub><sup>-</sup> and Bi<sup>3+</sup>/Bi<sup>5+</sup> redox mediators, *Appl. Catal. B Environ.* 284 (2021), 119808.
- [15] D. Majhi, Y.P. Bhoi, P.K. Samal, B.G. Mishra, Morphology controlled synthesis and photocatalytic study of novel CuS-Bi<sub>2</sub>O<sub>2</sub>CO<sub>3</sub> heterojunction system for chlorpyrifos degradation under visible light illumination, *Appl. Surf. Sci.* 455 (2018) 891–902.
- [16] J. Low, C. Jiang, B. Cheng, S. Wagh, A.A. Al-Ghamdi, J. Yu, A review of direct Z-scheme photocatalysts, *Small Methods* 1 (2017), 1700080.
- [17] L. Sun, J. Li, X. Li, C. Liu, H. Wang, P. Huo, Y.S. Yan, Molecularly imprinted Ag/Ag<sub>3</sub>VO<sub>4</sub>/g-C<sub>3</sub>N<sub>4</sub> Z-scheme photocatalysts for enhanced preferential removal of tetracycline, *J. Colloid Interface Sci.* 552 (2019) 271–286.
- [18] Y. Guo, Y. Ao, P. Wang, C. Wang, Mediator-free direct dual-Z-scheme Bi<sub>2</sub>S<sub>3</sub>/BiVO<sub>4</sub>/MgIn<sub>2</sub>S<sub>3</sub> composite photocatalysts with enhanced visible-light-driven performance towards carbamazepine degradation, *Appl. Catal. B Environ.* 254 (2019) 479–490.
- [19] Q.A. Drmosh, A. Hezam, A.H.Y. Hendi, M. Qamar, Z.H. Yamania, K. Byrapa, Ternary Bi<sub>2</sub>S<sub>3</sub>/MoS<sub>2</sub>/TiO<sub>2</sub> with double Z-scheme configuration as high performance photocatalyst, *Appl. Surf. Sci.* 499 (2020), 143938.

[20] W.K. Jo, N.C.S. Selvam, Z-scheme CdS/g-C<sub>3</sub>N<sub>4</sub> composites with RGO as an electron mediator for efficient photocatalytic H<sub>2</sub> production and pollutant degradation, *Chem. Eng. J.* 317 (2017) 913–924.

[21] X. Zhang, F. Tian, L. Qiu, M. Gao, W. Yang, Y. Liu, Y. Yu, Z-Scheme Mo<sub>2</sub>C/MoS<sub>2</sub>/In<sub>2</sub>S<sub>3</sub> dual-heterojunctions for the photocatalytic reduction of Cr(VI), *J. Mater. Chem. A* 9 (2021) 10297–10303.

[22] L. Jiang, X. Yuan, G. Zeng, J. Liang, X. Chen, H. Yu, H. Wang, Z. Wu, J. Zhang, T. Xiong, In-situ synthesis of direct solid-state dual Z-scheme WO<sub>3</sub>/g-C<sub>3</sub>N<sub>4</sub>/Bi<sub>2</sub>O<sub>3</sub> photocatalyst for the degradation of refractory pollutant, *Appl. Catal. B Environ.* 227 (2018) 376–385.

[23] P.J. Mafa, B. Ntsendwana, B.B. Mamba, A.T. Kuvarega, Visible light driven ZnMoO<sub>4</sub>/BiFeWO<sub>6</sub>/rGO Z-scheme photocatalyst for the degradation of anthraquinone dye, *J. Phys. Chem. C* 123 (2019) 20605–20616.

[24] M. Gao, L. Sun, C. Ma, X. Li, H. Jiang, D. Shen, H. Wang, P. Huo, Constructed Z-scheme g-C<sub>3</sub>N<sub>4</sub>/Ag<sub>3</sub>VO<sub>4</sub>/rGO photocatalysts with multi-interfacial electron-transfer paths for high photoreduction of CO<sub>2</sub>, *Inorg. Chem.* 60 (2021) 1755–1766.

[25] D. Majhi, K. Das, R. Bariki, S. Padhan, A. Mishra, R. Dhiman, P. Dash, B. Nayak, B. G. Mishra, A facile reflux method for in situ fabrication of a non-cytotoxic Bi<sub>2</sub>S<sub>3</sub>/β-Bi<sub>2</sub>O<sub>3</sub>/ZnIn<sub>2</sub>S<sub>4</sub> ternary photocatalyst: a novel dual Z-scheme system with enhanced multifunctional photocatalytic activity, *J. Mater. Chem. A* 8 (2020) 21729–21743.

[26] D. Majhi, K. Das, A. Mishra, R. Dhiman, B.G. Mishra, One pot synthesis of CdS/BiOBr/Bi<sub>2</sub>O<sub>3</sub>CO<sub>3</sub>: A novel ternary double Z-scheme heterostructure photocatalyst for efficient degradation of atrazine, *Appl. Catal. B Environ.* 260 (2020), 118222.

[27] G. A. Kallawar, D. P. Barai, B. A. Bhanwar, Bismuth titanate based photocatalysts for degradation of persistent organic compounds in wastewater: a comprehensive review on synthesis methods, performance as photocatalyst and challenges, *J. Clean. Prod.* 318 (2021), 128563.

[28] J. Lia, M. Han, Y. Guo, F. Wang, L. Meng, D. Mao, S. Ding, C. Sun, Hydrothermal synthesis of novel flower-like BiVO<sub>4</sub>/Bi<sub>2</sub>Ti<sub>2</sub>O<sub>7</sub> with superior photocatalytic activity toward tetracycline removal, *Appl. Catal. A: Gen.* 524 (2016) 105–114.

[29] K. Das, D. Majhi, Y.P. Bhoi, B.G. Mishra, Combustion synthesis, characterization and photocatalytic application of CuS/Bi<sub>4</sub>Ti<sub>3</sub>O<sub>12</sub> p-n heterojunction materials towards efficient degradation of 2-methyl-4-chlorophenoxyacetic acid herbicide under visible light, *Chem. Eng. J.* 362 (2019) 588–599.

[30] M. Grao, J. Redfern, P.J. Kelly, M. Ratova, Magnetron co-sputtered Bi<sub>12</sub>TiO<sub>20</sub>/Bi<sub>4</sub>Ti<sub>3</sub>O<sub>12</sub> composite – an efficient photocatalytic material with photoinduced oxygen vacancies for water treatment application, *Appl. Surf. Sci.* 552 (2021), 149486.

[31] X. Wang, Y. Wang, M. Gao, J. Shen, X. Pu, Z. Zhang, H. Lin, X. Wang, BiVO<sub>4</sub>/Bi<sub>4</sub>Ti<sub>3</sub>O<sub>12</sub> heterojunction enabling efficient photocatalytic reduction of CO<sub>2</sub> with H<sub>2</sub>O to CH<sub>3</sub>OH and CO, *Appl. Catal. B: Environ.* 270 (2020), 118876.

[32] W.N. Su, D.W. Ayele, V. Ochie, C.J. Pan, B.J. Hwang, The development of highly crystalline single-phase Bi<sub>20</sub>TiO<sub>32</sub> nanoparticles for light driven oxygen evolution, *Appl. Catal. B: Environ.* 150–151 (2014) 363–369.

[33] H. Cheng, B. Huang, Y. Dai, X. Qin, X. Zhang, Z. Wang, M. Jiang, Visible-light photocatalytic activity of the metastable Bi<sub>20</sub>TiO<sub>32</sub> synthesized by a high-temperature quenching method, *J. Solid State Chem.* 182 (2009) 2274–2278.

[34] J. Hou, Z. Wang, C. Yang, W. Zhou, S. Jiao, H. Zhu, Hierarchically plasmonic Z-scheme photocatalyst of Ag/AgCl nanocrystals decorated mesoporous single-crystalline metastable Bi<sub>20</sub>TiO<sub>32</sub> nanosheets, *J. Phys. Chem. C* 117 (2013) 5132–5141.

[35] L. Cheng, Q. Xiang, Y. Liao, H. Zhang, CdS-based photocatalysts, *Energy Environ. Sci.* 11 (2018) 1362–1391.

[36] X. Wu, J. Zhao, L. Wang, M. Han, M. Zhang, H. Wang, H. Huang, Y. Liu, Z. Kang, Carbon dots as solid-state electron mediator for BiVO<sub>4</sub>/Cds/CdS Z-scheme photocatalyst working under visible light, *Appl. Catal. B: Environ.* 206 (2017) 501–509.

[37] W.K. Jo, N.C.S. Selvam, Z-scheme CdS/g-C<sub>3</sub>N<sub>4</sub> composites with RGO as an electron mediator for efficient photocatalytic H<sub>2</sub> production and pollutant degradation, *Chem. Eng. J.* 317 (2017) 913–924.

[38] J. Zhang, Y. Guo, Y. Xiong, D. Zhou, S. Dong, An environmentally friendly Z-scheme WO<sub>3</sub>/CDots/CdS heterostructure with remarkable photocatalytic activity and anti-photocorrosion performance, *J. Catal.* 356 (2017) 1–13.

[39] T. Gfeizhou, J. Chenghu, Mass Production and photocatalytic activity of highly crystalline metastable single-phase Bi<sub>20</sub>TiO<sub>32</sub> nanosheets, *Environ. Sci. Technol.* 44 (2010) 8698–8703.

[40] Anu K. Yadav, Optical and dielectric properties of Bi<sub>2</sub>Ti<sub>2</sub>O<sub>7</sub>/Bi<sub>4</sub>Ti<sub>3</sub>O<sub>12</sub> nanocomposite, *Mater. Today: Proc.* 28 (2020) 153–157.

[41] L. Wang, H. Li, S. Zhang, Y. Long, L. Li, Z. Zheng, S. Wu, L. Zhou, Y. Hei, L. Luo, F. Jiang, One-step synthesis of Bi<sub>4</sub>Ti<sub>3</sub>O<sub>12</sub>/Bi<sub>2</sub>O<sub>3</sub>/Bi<sub>12</sub>TiO<sub>20</sub> spherical ternary heterojunction with enhanced photocatalytic properties via sol-gel method, *Solid State Sci.* 100 (2020), 106098.

[42] X.Y. Yu, X.W. Lou, Mixed metal sulfides for electrochemical energy storage and conversion, *Adv. Energy Mater.* (2017), 1701592.

[43] P. Sathishkumar, K. Mohan, A.R. Ganesan, M. Govarthanan, A.R.M. Yusoff, F.L. Gu, Persistence, toxicological effect and ecological issues of endosulfan – a review, *J. Hazard. Mater.* 416 (2021), 125779.

[44] A. Mudhoo, A. Bhatnagar, M. Rantankila, V. Srivastava, M. Sillanpa, Endosulfan removal through bioremediation, photocatalytic degradation, adsorption and membrane separation processes: a review, *Chem. Eng. J.* 360 (2019) 912–928.

[45] V.K. Gupta, I. Ali, Removal of endosulfan and methoxychlor from water on carbon slurry, *Environ. Sci. Technol.* 42 (2008) 766–770.

[46] R. Rani, V. Kumar, P. Gupta, A. Chandra, Potential use of *Solanum lycopersicum* and plant growth promoting rhizobacterial (PGPR) strains for the phytoremediation of endosulfan stressed soil, *Chemosphere* 279 (2021), 130589.

[47] L. Kong, S. Zhu, L. Zhu, H. Xie, K. Su, T. Yan, J. Wang, J. Wang, F. Wang, F. Sun, Biodegradation of organochlorine pesticide endosulfan by bacterial strain *Alcaligenes faecalis* JBW4, *J. Environ. Sci.* 25 (2013) 2257–2264.

[48] M.R. Pena, J.A. Barrios, E.B. Bravo, M.A. Rodrigo, C.E.B. Diaz, Degradation of endosulfan by a coupled treatments in a batch reactor with three electrodes, *Fuel* 281 (2020), 118741.

[49] N.S. Shah, X. He, J.A. Khan, H.M. Khan, D.L. Boccelli, D.D. Dionysiou, Comparative studies of various iron-mediated oxidative systems for the photochemical degradation of endosulfan in aqueous solution, *J. Photochem. Photobiol. A: Chem.* 306 (2015) 80–86.

[50] K. Sivagami, B. Vikraman, R. Ravi Krishna, T. Swaminathan, Chlorpyrifos and Endosulfan degradation studies in an annular slurry photo reactor, *Ecotoxicol. Environ. Saf.* 134 (2016) 327–331.

[51] B. Xiong, A. Zhou, G. Zheng, J. Zhang, W. Xu, Photocatalytic degradation of endosulfan in contaminated soil with the elution of surfactants, *J. Soils Sediment.* 15 (2015) 1909–1918.

[52] A.M. Ismael, A.N. El-Shazly, S.E. Gaber, M.M. Rashad, A.H. Kamel, S.S.M. Hassan, Novel TiO<sub>2</sub>/GO/CuFe<sub>2</sub>O<sub>4</sub> nanocomposite: a magnetic, reusable and visible-light-driven photocatalyst for efficient photocatalytic removal of chlorinated pesticides from wastewater, *RSC Adv.* 10 (2020) 34806–34814.

[53] P. Devaraji, M. Mapa, H.M.A. Hakkeem, V. Sudhakar, K. Krishnamoorthy, C. S. Gopinath, ZnO-ZnS heterojunctions: a potential candidate for optoelectronics applications and mineralization of endocrine disruptors in direct sunlight, *ACS Omega* 2 (2017) 6768–6781.

[54] S.R. Jain, K.C. Adiga, V.R. Verneker, A new approach to thermochemical calculations of condensed fuel-oxidizer mixtures, *Combust. Flame* 40 (1981) 71–79.

[55] T. Siddique, B.C. Okeke, M. Arshad, W.T. Frankenberger, Biodegradation kinetics of endosulfan by *Fusarium ventricosum* and a *Pandoraea* species, *J. Agric. Food Chem.* 51 (2003) 8015–8019.

[56] P.F. Smet, J.V. Gheluwe, D. Poelman, R.L.V. Meirhaeghe, Photoluminescence of electron beam evaporated CaS:Bi thin films, *J. Lumin.* 104 (2003) 145–150.

[57] Q. Xiao, J. Zhang, C. Xiao, X. Tan, Photocatalytic degradation of methylene blue over Co<sub>3</sub>O<sub>4</sub>/Bi<sub>2</sub>WO<sub>6</sub> composite under visible light irradiation, *Catal. Commun.* 9 (2008) 1247–1253.

[58] M. Zhu, S. Kim, L. Mao, M. Fujitsuka, J. Zhang, X. Wang, T. Majima, Metal-free photocatalyst for H<sub>2</sub> evolution in visible to near-infrared region: black phosphorus/graphitic carbon nitride, *J. Am. Chem. Soc.* 139 (2017) 13234–13242.

[59] Z.C. Ling, H.R. Xia, W.L. Liu, H. Hand, X.Q. Wang, S.Q. Sun, D.G. Ran, L.L. Yu, Lattice vibration of bismuth titanate nanocrystals prepared by metalorganic decomposition, *Mater. Sci. Eng. B* 128 (2006) 156–160.

[60] P. Duraan, F. Capel, C. Moure, M. Villegas, J.F. Fernaandez, J. Tartaj, A. C. Caballero, Processing and dielectric properties of the mixed-layer bismuth titanate niobate Bi<sub>7</sub>Ti<sub>4</sub>NbO<sub>21</sub> by the metal-organic precursor synthesis method, *J. Eur. Ceram. Soc.* 21 (2001) 1–8.

[61] A.R. West, Solid State Chemistry and its Application, John Wiley & Sons Pte Ltd, Singapore, 1998, pp. 115–186.

[62] R. Zhao, T. Yang, Y. Luo, M. Chuai, X. Wu, Y. Zhang, Y. Ma, M. Zhang, Structural phase transition and photoluminescence properties of wurtzite CdS:Eu<sup>3+</sup> nanoparticles under high pressure, *RSC Adv.* 7 (2017) 31433–31440.

[63] B. Shi, H. Yin, J. Gong, Q. Nie, Ag/AgCl decorated Bi<sub>4</sub>Ti<sub>3</sub>O<sub>12</sub> nanosheet with highly exposed (001) facets for enhanced photocatalytic degradation of Rhodamine B, Carbamazepine and Tetracycline, *Appl. Surf. Sci.* 419 (2017) 614–623.

[64] D. Hou, X. Hu, Y. Wen, B. Shan, P. Hu, X. Xiong, Y. Qiao, Y. Huang, Electrosyn silenite Bi<sub>12</sub>MO<sub>20</sub> (M = Ti, Ge, Si) nanofibers: general synthesis, band structure, and photocatalytic activity, *Phys. Chem. Chem. Phys.* 15 (2013) 20698–20705.

[65] H. Li, L. Liu, Z. Wang, X. Zheng, S. Meng, S. Chen, X. Fu, Optimizing the precursor of sulfur source for hydrothermal synthesis of high performance CdS for photocatalytic hydrogen production, *RSC Adv.* 8 (2018) 11489–11497.

[66] A. Ishikawa, T. Takata, J.N. Kondo, M. Hara, H. Kobayashi, K. Domen, Oxsulfide Sm<sub>2</sub>Ti<sub>2</sub>S<sub>2</sub>O<sub>5</sub> as a stable photocatalyst for water oxidation and reduction under visible light irradiation ( $\lambda \leq 650$  nm), *J. Am. Chem. Soc.* 124 (2002) 13547–13553.

[67] D. Majhi, P.K. Samal, K. Das, S.K. Gouda, Y.P. Bhoi, B.G. Mishra,  $\alpha$ -NiS/Bi<sub>2</sub>O<sub>3</sub> Nanocomposites for enhanced photocatalytic degradation of tramadol, *ACS Appl. Nano Mater.* 2 (2019) 395–407.

[68] S. Obregon, M.A. Ruiz-Gomez, D.B. Hernandez-Uresti, Direct evidence of the photocatalytic generation of reactive oxygen species (ROS) in a Bi<sub>2</sub>W<sub>2</sub>O<sub>9</sub> layered-structure, *J. Colloid Interface Sci.* 506 (2017) 111–119.

[69] X. Ning, J. Li, B. Yang, W. Zhen, Z. Li, B. Tian, G. Lu, Inhibition of photocorrosion of CdS via assembling with thin film TiO<sub>2</sub> and removing formed oxygen by artificial gill for visible light overall water splitting, *Appl. Catal. B: Environ.* 212 (2017) 129–139.